On the False Alarm Probability of the Normalized Matched Filter for Off-Grid Targets: A Geometrical Approach and Its Validity Conditions

Pierre Develter, Jonathan Bosse, Olivier Rabaste, Philippe Forster, and Jean-Philippe Ovarlez

***Abstract*—Off-grid targets are known to induce a mismatch that dramatically impacts the detection probability of the popular Normalized Matched Filter. To overcome this problem, the unknown target parameter is usually estimated through a Maximum Likelihood strategy, resulting in a GLRT (Generalized Likelihood Ratio Test) detection scheme. While the test statistic for the null hypothesis is well known in the on-grid case, the off-grid scenario is more involved, and to the best of our knowledge, no such theoretical result is available. This paper fills this gap by proposing such an expression under circular compound Gaussian noise with a known covariance matrix thanks to a geometrical approach. It is exact, provided that the probability of false alarm is low enough: we derive the conditions guaranteeing the exactness of the relationship, and we show numerically that the formula still yields a good approximation of the probability of false alarm when this condition is not met.**

***Index Terms*—Radar detection, off-grid, GLRT, P_{FA}-threshold relationship, theory of tubes.**

I. Introduction

In domains as varied as telecommunications, psychology, or radar, detection theory is crucial to separate ambient noise from signals of interest. In detection theory, received signals are submitted to a hypothesis test to discriminate useful signals from noise. Detection of signals with unknown deterministic parameters is classically addressed with a Generalized Likelihood Ratio Test (GLRT) that replaces the unknown parameters with their Maximum Likelihood Estimators (MLE) in the Likelihood Ratio detection test [1]. When analytical MLE solutions are not available for signal parameters of interest, most detection strategies assume for ease of implementation that those parameters lie over a discrete set, called the grid, usually chosen so that all tests on the grid are statistically independent when the tested signal consists of noise. However, parameters have no reason to fall precisely on the grid since they are often distributed over a continuous range. This induces an off-grid mismatch between the tested and true target parameters that deteriorates the detection performance of most state-of-the-art tests made under the on-grid assumption. This paper will consider this very general problem in the radar context where unknown parameters can include Doppler shift, distance, or direction without loss of generality. The Normalized Matched Filter is the GLRT associated with the problem of detecting a known signal of unknown amplitude in Gaussian ambient noise of unknown power. It is also widely used for adaptive radar in non-Gaussian contexts [2] for example when the noise is distributed according to a Complex Elliptically Symmetric (CES) distribution [3]. The off-grid mismatch impact is particularly dramatic for the Normalized Matched Filter (NMF) test [4]. In some cases, the detection probability may even vanish to 0 when the Signal-to-Noise Ratio (SNR) tends to infinity [4], especially for low Probabilities of False Alarm (P_{FA}), familiar in radar context. To overcome this problem, the most apparent solution consists of testing over the whole continuous support of the signal parameter, not just the grid: this is the "true" GLRT, that we call "off-grid GLRT" or "off-grid NMF" in this paper. However, to the best of our knowledge, the analytical expression of the null hypothesis statistic and the related P_{FA} is unknown in the literature for this GLRT.

The robustness of detectors to mismatched signals is a well-explored topic in the detection literature. Several types of mismatches are addressed thanks to the derivation of suited GLRTs, such as mismatch lying in a cone [5], [6], [7], [8], extended to include the possibility of a mismatched interference signal in [9], quadratically constrained [10], among others [11]. Sometimes, another approach is privileged, and other signal models are used to reduce interference from orthogonal signals [12]. Those works deal with a general mismatch model, that can be used to model several events, such as pointing errors, imperfect array calibration, or multipath distortion. However, those mismatch models and the associated detectors do not suit the very specific non-linear off-grid mismatch well. For example, to fit an entire cell in a cone, a lot of unwanted signals must be included in the acceptance zone of the detector, thus decreasing its selectivity. Furthermore, the low P_{FA} used in

Manuscript received 24 April 2023; revised 27 November 2023; accepted 8 January 2024. Date of publication 25 January 2024; date of current version 20 February 2024. The associate editor coordinating the review of this manuscript and approving it for publication was Dr. Augusto Aubry. *(Corresponding author: Pierre Develter.)*

Pierre Develter and Jean-Philippe Ovarlez are with DEMR, ONERA, Université Paris-Saclay, F-91120 Palaiseau, France, and also with SONDRA, Centrale-Supélec, Université Paris-Saclay, F-91192 Gif-sur-Yvette, France (e-mail: pierre.develter@onera.fr).

Jonathan Bosse and Olivier Rabaste are with DEMR, ONERA, Université Paris-Saclay, F-91120 Palaiseau, France.

Philippe Forster is with the Université Paris-Saclay, ENS Paris-Saclay, CNRS, SATIE, F-91190 Gif-sur-Yvette, France.

Digital Object Identifier 10.1109/TSP.2024.3358621

Radar context makes things even harder: the cone approach is limited to high P_{FA} to deal with off-grid targets, which is not always realistic in practice [13].

While the off-grid issue has been studied extensively in inverse reconstruction problems [14], [15] (in those contexts, the decrease in performance due to off-grid targets is particularly dramatic) and in sparse estimation problems (especially in off-grid Direction Of Arrival estimation in Radar contexts, see for example [16], [17]), off-grid target detection has received less interest as far as we are aware of.

In the Bayesian context, when all target parameters are distributed according to a uniform probability distribution, it can be shown that the best detector in the sense of the average probability of detection is the Average Likelihood Ratio Test (ALRT) derived in [18] assuming the signal amplitude as known and in [19] assuming a random Gaussian signal amplitude.

This paper focuses on the deterministic case where the target amplitude and unknown parameters are deterministic. In this context, the off-grid GLRT can be costly to implement with satisfying precision and is hard to analyze. For this reason, sometimes the problem is simplified: for example, the steering vector can be made linear concerning the mismatch with a first-order Taylor approximation, making it possible to derive analytical forms for the simplified GLRT, offering good detection performance, although the P_{FA}-threshold relationship is unknown [20], [21]. Another approach to simplify the problem consists of modeling the cell as a linear subspace with Discrete Spheroidal Sequences subspace [4] or the Taylor expansion of the signal [22]: this allows for the use of subspace detectors [23]. In this case, theoretical analysis of the test is easy to perform, but detection performance is considerably lower than the off-grid GLRT, especially under non-white noise contexts [24].

This paper studies the "true" off-grid GLRT without approximation, as was done in [25] in the adaptive case. Our aim is not the implementation but rather the analysis of the off-grid GLRT, which is often delicate. In particular, the theoretical P_{FA} is difficult to investigate since the test quantity is the maximum of non-independent random variables. Yet, it is essential as it is needed to implement the detector.

The search for the probability of a stochastic process or random field exceeding a threshold has been the subject of numerous works in the applied statistics literature (see, for example, [26], [27], [28]). However, those works mainly focus on real processes and random fields, and to our knowledge, few articles [29] link them with the detectors used by the signal processing community.

Based on earlier results on the volume of tubes on sphere [30], [31], we showed in [32] how to obtain an upper bound for the P_{FA}-threshold relationship. In this paper, we dive once again into tube theory to show how it also enables an original and simple derivation of the on-grid P_{FA}-threshold relationship. Moreover, starting from studies on overlap [33], [34] we derive new conditions of equality of the proposed upper bound. We show that above a certain limit threshold, equality is met. Closed-form expressions for this limit threshold are derived under white noise. As we will show, the proposed formula is proved to be exact under P_{FA}s that are not too high, which is the standard regime of application of the NMF.

Section II presents the signal model, the off-grid problem, and the true GLRT formulation. Section III introduces the tube formalism and gives an original derivation of the P_{FA}-threshold relationship using a formula related to the surface of tubes embedded on hyper-spheres. Section IV showcases the domain of validity of the relationship. It features the derivation of local overlap criteria for tubes around general multi-dimensional manifolds embedded on hyper-spheres. In Section V we check the validity of our derivations for our application by comparing the theoretical thresholds to Monte-Carlo simulations. The relationship between the correlation of the noise and the size of the domain of validity is also examined.

Notations: Matrices are in bold and capital, vectors in bold. For any matrix $\mathbf{A}$ or vector, $\mathbf{A}^T$ is the transpose of $\mathbf{A}$ and $\mathbf{A}^H$ is the Hermitian transpose of $\mathbf{A}$. $\mathbf{I}$ is the $N \times N$ identity matrix and $\mathcal{CN}(\boldsymbol{\mu}, \boldsymbol{\Gamma})$ is the circular complex Normal distribution of mean $\boldsymbol{\mu}$ and covariance matrix $\boldsymbol{\Gamma}$. $\mathbb{S}^{n-1}$ is the unit sphere in $\mathbb{R}^n$. The real and imaginary part operators of a complex number are denoted by $\mathrm{Re}(.)$ and $\mathrm{Im}(.)$. The operator $\angle u$ is the angle of a complex number u. $\odot$ denotes the Hadamard product. $\Gamma(.)$ is the gamma function. $\|.\|$ denotes the classical l_2 norm for vectors.

II. Problem Formulation

A. Signal Model

A very common detection problem in radar as well as in other domains consists of detecting a complex signal $\mathbf{d} \in \mathbb{C}^N$ corrupted by an additive noise $\mathbf{n}$ (clutter, thermal noise, etc.). This problem can be stated as the following binary hypothesis test, where the goal consists of deciding between two hypotheses H_0 and H_1:

$$\begin{cases} H_0 : \mathbf{r} = \mathbf{n}, & \text{(noise only)} \\ H_1 : \mathbf{r} = \alpha\, \mathbf{d}(\theta) + \mathbf{n}, & \text{(signal plus noise)} \end{cases}$$

where $\mathbf{r}$ is the complex vector of size N of the sampled received signal, α is an unknown complex target amplitude and $\mathbf{d}(\theta)$ stands for a generally known *steering vector* characterized by unknown target parameters θ (time-delay, Doppler or angle in radar). In the sequel, we will assume that $\mathbf{n}$ is a zero-mean complex circular Gaussian noise vector with unknown variance σ^2 i.e. $\mathbf{n} \sim \mathcal{CN}(\mathbf{0}, \sigma^2\, \boldsymbol{\Gamma})$ and known shape matrix $\boldsymbol{\Gamma}$ (covariance matrix up to a scale factor). This context is known as a partially homogeneous Gaussian environment. All the results in this paper still apply to any other spherically invariant distribution. In this work, we will assume θ to be a deterministic unknown scalar. Although all general results of this paper apply to any signal model $\mathbf{d}(\theta)$ (including chirp signals, in which case the unknown parameter θ models the unknown range of the target), to derive closed-form solutions, we choose the following common signal model:

$$\mathbf{d}(\theta) = \frac{1}{\sqrt{N}} \left[1, e^{2i\pi\theta}, \ldots, e^{2i\pi(N-1)\theta}\right]^T. \tag{1}$$

This model of steering vector is very common in spectral analysis and often encountered in radar Range-Doppler

detection schemes (in which case θ represents the Doppler shift of the target) where the problem consists in estimating a complex sinusoid embedded in noise after range Matched Filter processing.

B. Normalized Matched Filter (NMF)

In classical detection theory, for unknown parameters $\{\boldsymbol{\lambda}_i\}_{i\in[0,1]}$ depending on each hypothesis $\{H_i\}_{i\in[0,1]}$ (either parameters of interest, and/or nuisance parameters), the usual procedure relies on the Generalized Likelihood Ratio (GLR) statistic, namely the ratio $\Lambda(\mathbf{r})$ between the Probability Density Function (PDF) $f_{H_1}(.)$ of the data under H_1 and the PDF $f_{H_0}(.)$ under H_0 where the unknown parameters are replaced by their ML estimate:

$$\Lambda(\mathbf{r}) = \frac{\max_{\boldsymbol{\lambda}_1} f_{H_1}(\mathbf{r})}{\max_{\boldsymbol{\lambda}_0} f_{H_0}(\mathbf{r})} \underset{\mathrm{H_0}}{\overset{\mathrm{H_1}}{\gtrless}} w^2,$$

where w^2 is the detection threshold set according to a desired P_{FA}, such that:

$$P_{FA} = \int_{D_A} f_{H_0}(\mathbf{r}) d\mathbf{r}, \tag{2}$$

where $D_A \subset \mathbb{R}^N$ is the *domain of acceptance* of the test, defined as $D_A = \{\mathbf{r} \in \mathbb{R}^N : \Lambda(\mathbf{r}) > w^2\}$.

When $\boldsymbol{\lambda}_1 = \{\alpha, \sigma\}$ and $\boldsymbol{\lambda}_0 = \{\sigma\}$ with θ known, the corresponding GLRT is known as the NMF (Normalized Matched Filter) [1]:

$$\frac{\left|\mathbf{d}(\theta)^H \boldsymbol{\Gamma}^{-1} \mathbf{r}\right|^2}{\left(\mathbf{d}(\theta)^H \boldsymbol{\Gamma}^{-1} \mathbf{d}(\theta)\right)\left(\mathbf{r}^H \boldsymbol{\Gamma}^{-1} \mathbf{r}\right)} \underset{\mathrm{H_0}}{\overset{\mathrm{H_1}}{\gtrless}} w^2. \tag{3}$$

This test is also widely used for adaptive radar in non-Gaussian contexts [2], [35] for example, when the noise is distributed according to a Complex Elliptically Symmetric (CES) distribution [3]. Its statistic under H_0, in this case, is the same as in the Gaussian case.

Equivalently, Eq. (3) can be rewritten with normalized whitened vectors:

$$\left|\mathbf{s}(\theta)^H \mathbf{u}\right|^2 \underset{\mathrm{H_0}}{\overset{\mathrm{H_1}}{\gtrless}} w^2, \tag{4}$$

where $\mathbf{s}(\theta) = \dfrac{\boldsymbol{\Gamma}^{-1/2}\mathbf{d}(\theta)}{\left\|\boldsymbol{\Gamma}^{-1/2}\mathbf{d}(\theta)\right\|}$ and $\mathbf{u} = \dfrac{\boldsymbol{\Gamma}^{-1/2}\mathbf{r}}{\left\|\boldsymbol{\Gamma}^{-1/2}\mathbf{r}\right\|}$.

The corresponding P_{FA}-threshold relationship is well known and is found using statistical tools in [1]:

$$P_{FA} = \left(1 - w^2\right)^{N-1}. \tag{5}$$

Note that the NMF expression (4) has a simple geometric interpretation. It is indeed the squared cosine of the angle between $\mathbf{s}(\theta)$ and $\mathbf{u}$. The threshold characterizes the squared cosine of the angle $\cos^{-1} w$. A target is detected when the vector angle is below this limit angle.

C. Detecting on a Grid and Related Issues

The test (4) was derived with the parameter θ supposed to be known. In practice, this is not the case, and this is why tests are made for several fixed parameter values. The collection of parameters θ where detection tests are run is called the grid. For our model, the usual grid is generally $\mathcal{G} = \left\{ \dfrac{k}{N} : k \in [0, 1, \ldots, N-1] \right\}$. Fourier resolution cells for this grid are then the following

$$\mathcal{D}_k = \left[\frac{k}{N} - \frac{0.5}{N}, \frac{k}{N} + \frac{0.5}{N}\right], \tag{6}$$

where $k \in [0, 1, \ldots, N-1]$.

When the point θ where the NMF is tested is different from the target's true parameter θ_0, the target is said to be off-grid. This induces a mismatch $\delta_\theta = \theta - \theta_0$ between the true target steering vector $\mathbf{s}(\theta_0)$ and the steering vector $\mathbf{s}(\theta)$ under test. Unfortunately, it was shown in [36] that the NMF detector is very sensitive to steering vector mismatch, potentially leading to a dramatic deterioration of the detection performance: the detection probability can even tend to 0 when the SNR tends to infinity. This phenomenon occurs [4] for P_{FA} as high as 10^{-3} in the chosen resolution cell of width $1/N$. Fig. 1 represents the average probability of detection of the NMF as a function of the SNR for δ_θ uniformly distributed in $\mathcal{D}_0$: the asymptotic probability is well below 1 for a threshold corresponding to a P_{FA} of 10^{-6}. Note that this simulation was done under white noise. The NMF behavior can be even worse when $\boldsymbol{\Gamma} \neq \mathbf{I}$. In this case, the detection probability depends on the considered cell $\mathcal{D}_k$.

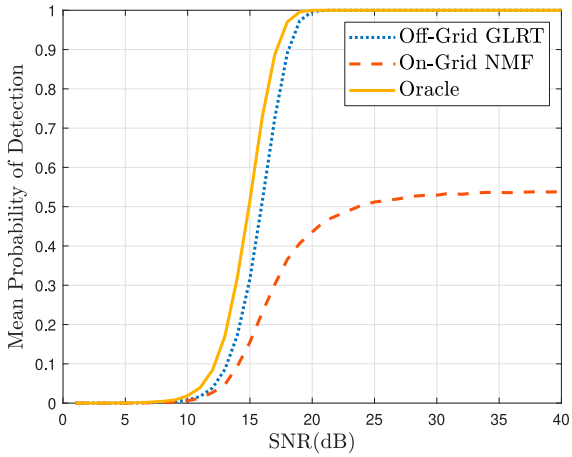

Fig. 1. Mean P_D of the standard on-grid NMF (4) (red), its oracle counterpart that knows the positions of the targets (yellow) and the off-grid GLRT (7) (blue) as a function of the SNR in the presence of off-grid targets under white noise. $P_{FA} = 10^{-6}$ and $N = 10$.

D. The Off-Grid GLRT

Instead of assuming that the target parameter lies on a grid, it is more realistic to assume that it is unknown. This leads to the general off-grid GLRT procedure, which gives in our case:

$$GLRT(\mathbf{u}, \mathcal{D}) = \max_{\theta \in \mathcal{D}} \left|\mathbf{s}(\theta)^H \mathbf{u}\right|^2 \underset{\mathrm{H_0}}{\overset{\mathrm{H_1}}{\gtrless}} w^2, \tag{7}$$

where $\mathcal{D}$ is the search domain relative to the unknown parameter θ. Usually, for the steering vector defined in Eq. (1), $\mathcal{D}$ is defined as one of the Fourier resolution cells $\mathcal{D}_k$.

This detector corrects the off-grid issue of test (4) as can be seen in Fig. 1: its probability of detection is close to that of the oracle detector that knows the positions of the targets.

There are several ways to approximate the test quantity (7). The most natural solution consists of refining the search grid. However, the computational cost may become high for a precise estimation of the test quantity, as the number of tests to be run to approximate (7) equals the oversampling factor. A more clever approach uses joint detection and estimation tools, which jointly merge the detection and estimation steps in the signal processing chain. The unknown parameter is estimated, not necessarily in the MLE sense, then introduced in the test quantity (3). Examples of estimation techniques that may be used to estimate the target parameter in this procedure include monopulse-based techniques [24] or the interpolation of the Fourier Transform lobe [37]. This empirical approach enables a precise approximation of the target parameter at a low computational cost, similar to oversampling by a factor of two, even under colored noise [24]. Finally, maximizing for the unknown parameter was shown to be a semi-definite positive convex problem in [25] so that interior point methods can achieve the required precision in polynomial time in N.

This paper is a theoretical analysis of the off-grid NMF, where we assume that the test quantity (7) is computed exactly. More specifically, we aim to derive its P_{FA}-threshold relationship. Indeed, the threshold w^2 to be used in (7) is different from the one in (3), because while the PDF f_{H_0} of the noise does not change in (2) whether we consider (7) or (3), the domain of acceptance D_A does. The difficulty consists here of evaluating the statistic of the maximum of a continuum of non-independent random variables.

III. An Analytical P_{FA}-Threshold Relationship With a Geometrical Interpretation

Through geometrical considerations, Hotelling [30] derived a methodology to study statistical tests over the real sphere thanks to the computation of the surfaces of tubes around a curve. Indeed, for a spherically invariant noise on the sphere, evaluating the P_{FA} of a test reduces to computing the surface of the acceptance zones, which are tubes. Section III-A presents his formula for the surface of tubes. It enables us to provide an alternative derivation of the well-known P_{FA}-threshold relationship (5) for the NMF in Section III-C thanks to a simple rewriting of the NMF test quantity in Section III-B. Unfortunately, as explained in Section III-D, Hotelling's formula cannot be directly applied to the case of the off-grid NMF expressed in (7). Indeed, as we will show, finding the P_{FA} in the radar case with one unknown parameter requires the computation of the volume of a tube around a manifold of dimension $M = 2$: this is addressed in Section III-D thanks to [31].

A. Hotelling's Original Geometrical Approach

This section presents Hotelling's original theorem for computing the surface of tubes on a sphere. Consider a curve $\boldsymbol{\gamma}(\xi)$ on the sphere $\mathbb{S}^{n-1}$, with $\xi \in [0, b]$. A tube $\mathcal{T}$ of geodesic radius ϕ is defined as the set of points with a geodesic distance to the curve inferior to ϕ. Formally:

$$\mathcal{T} = \left\{ \mathbf{u} \in \mathbb{S}^{n-1} : \exists \xi \in [0, b], \mathbf{u}^T \boldsymbol{\gamma}(\xi) > \cos(\phi) \right\}.$$

$\mathcal{T}$ can be seen as the union of the spherical caps $\mathcal{SC}_\xi = \left\{ \mathbf{u} \in \mathbb{S}^{n-1}, \mathbf{u}^T \boldsymbol{\gamma}(\xi) > \cos(\phi) \right\}$. Fig. 2 provides a graphical example of a tube. In [30], Hotelling gives a formula for computing the surface of $\mathcal{T}$ for a closed curve ($\boldsymbol{\gamma}(0) = \boldsymbol{\gamma}(b)$).

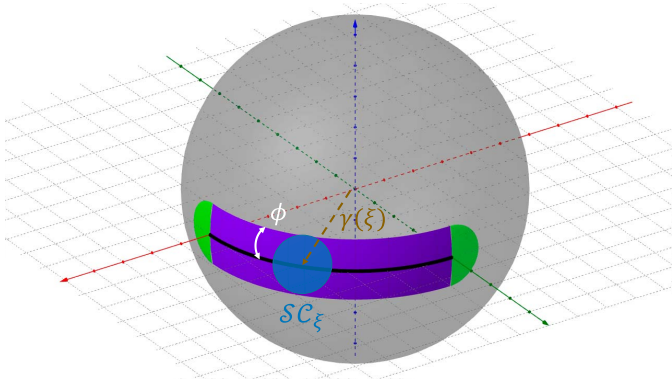

Fig. 2. Example of a tube $\mathcal{T}$ on $\mathbb{S}^2$ around a curve $\boldsymbol{\gamma}(\xi)$. Since the curve is non-closed, semi-spherical caps (in green) appear at the ends of $\mathcal{T}$.

Theorem III.1: [30] The surface enclosed by a tube of geodesic radius ϕ around a closed curve on the real unit sphere $\mathbb{S}^{n-1}$ is the product of the length of the axial curve by the volume of the $n-2$ ball of radius $\sin\phi$:

$$\frac{\pi^{(n-2)/2}}{\Gamma\left(\frac{n}{2}\right)} \sin^{n-2}(\phi). \tag{8}$$

When dealing with a non-closed curve, one has to add the surface of the two end semi-spherical caps to Hotelling's formula to characterize the surface of $\mathcal{T}$.

Note that, in general, for Hotelling's formula to hold, each point in the tube must belong to a unique cross-section. Following Hotelling, this restriction will be called the non-overlap condition. Overlap phenomenons can happen when a tube draws back into itself (non-local overlap) and its curvature becomes too high (local overlap). Non-overlap is locally guaranteed when ϕ is low enough. More specifically, for a curve of constant radius of curvature ρ, Hotelling shows in [30] that the condition for having no local overlap is the following:

$$\sin\phi \leq \rho. \tag{9}$$

In case of overlap, the surface given by Hotelling's theorem becomes an upper bound.

A study of overlap phenomenon is given in Section IV.

B. The Complex Manifold

This section aims to rewrite the NMF test quantity (4) using real vectors to apply Hotelling's formula (8). Indeed, for any $\alpha \in [0, 2\pi]$, let us remark that $\mathrm{Re}\left(\mathbf{s}(\theta)^H \mathbf{u} \exp(-i\alpha)\right) \leq \left|\mathbf{s}(\theta)^H \mathbf{u}\right|$, those two quantities being equal for $\alpha = \underline{\angle \mathbf{s}(\theta)^H \mathbf{u}}$.

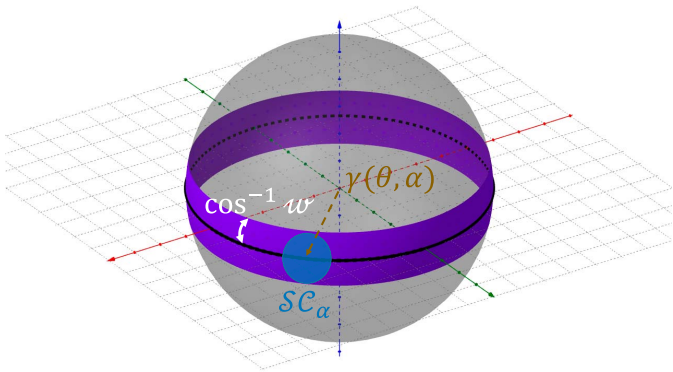

Fig. 3. $\mathcal{T}_{\text{on-grid}}$ (in violet) embedded on the unit sphere $\mathbb{S}^2$ in $\mathbb{R}^3$. $\mathcal{SC}_\alpha$ is drawn in blue [38].

We then have, decomposing $\mathbf{s}(\theta)$ and $\mathbf{u}$ into real and imaginary parts:

$$\text{Re}\left(\mathbf{s}(\theta)^H \mathbf{u} e^{-i\alpha}\right) = \left(\boldsymbol{\gamma}_1(\theta)^T \underline{\mathbf{u}}\right)\cos\alpha + \left(\boldsymbol{\gamma}_2(\theta)^T \underline{\mathbf{u}}\right)\sin\alpha\,,$$

where $\boldsymbol{\gamma}_1(\theta) = \begin{bmatrix}\text{Re}(\mathbf{s}(\theta))\\ \text{Im}(\mathbf{s}(\theta))\end{bmatrix}$, $\boldsymbol{\gamma}_2(\theta) = \begin{bmatrix}-\text{Im}(\mathbf{s}(\theta))\\ \text{Re}(\mathbf{s}(\theta))\end{bmatrix}$ and $\underline{\mathbf{u}} = \begin{bmatrix}\text{Re}(\mathbf{u})\\ \text{Im}(\mathbf{u})\end{bmatrix}$ is a $2N$-real valued noise vector drawn uniformly on $\mathbb{S}^{2N-1}$ under H_0. Denoting

$$\boldsymbol{\gamma}(\theta,\alpha) = \boldsymbol{\gamma}_1(\theta)\cos\alpha + \boldsymbol{\gamma}_2(\theta)\sin\alpha\,, \tag{10}$$

we have, therefore:

$$\max_{\alpha\in[0,2\pi]} \boldsymbol{\gamma}(\theta,\alpha)^T \underline{\mathbf{u}} = \left|\mathbf{s}(\theta)^H \mathbf{u}\right|\,. \tag{11}$$

We see that the complex case leads to consider a 2D real manifold $\gamma(\theta,\alpha)$. The GLRT (7) reads:

$$\max_{\theta,\alpha} \boldsymbol{\gamma}(\theta,\alpha)^T \underline{\mathbf{u}} \underset{H_0}{\overset{H_1}{\gtrless}} w\,. \tag{12}$$

C. An Original Alternative Derivation of the On-Grid PFA-Threshold Relationship

In this section, we provide a simple alternative derivation to [1] for the on-grid P_{FA} of (4). Indeed, finding the P_{FA} reduces to a simple geometrical problem, which enables us to apply Hotelling's theorem. Readers interested in the derivation of the P_{FA} for the GLRT (7) can skip to Section III-D. In this section, θ is considered fixed in $\mathcal{D}$: we deal with the on-grid case.

A false alarm occurs when $\underline{\mathbf{u}} \in \mathcal{T}_{\text{on-grid}}$, where

$$\mathcal{T}_{\text{on-grid}} = \left\{\underline{\mathbf{u}} \in \mathbb{S}^{2N-1} : \max_{\alpha\in[0,2\pi]} \boldsymbol{\gamma}(\theta,\alpha)^T \underline{\mathbf{u}} > w\right\}.$$

The tube $\mathcal{T}_{\text{on-grid}}$ we deal with here is represented in Fig. 3 in $\mathbb{R}^3$. Note that $\mathcal{T}_{\text{on-grid}}$ is drawn around a closed curve: indeed $\boldsymbol{\gamma}(\theta,0) = \boldsymbol{\gamma}(\theta,2\pi)$.

Since $\mathbf{u}$ has been whitened, $\underline{\mathbf{u}}$ is uniformly distributed over the unit $2N$-sphere under the null hypothesis, the P_{FA} is the ratio of the surface of $\mathcal{T}_{\text{on-grid}}$ and the surface of the unit sphere.

We can apply Theorem III.1 to the tube $\mathcal{T}_{\text{on-grid}}$ previously defined around the curve $\boldsymbol{\gamma}(\theta,\alpha)$ with fixed θ and parameterized by α to find the P_{FA} of the NMF (5). The length of the axial curve is equal to 2π. In this case, the tube is closed, and one does not need to add end spherical caps to Hotelling's formula. Furthermore, we prove that $\mathcal{T}_{\text{on-grid}}$ does not overlap in Section A of the appendix so that the surface given by Hotelling's formula is thus exact in this case. Applying Theorem III.1 with $n = 2N$, $\phi = \cos^{-1} w$ gives:

$$\begin{aligned}\text{Surface}(\mathcal{T}_{\text{on-grid}}) &= 2\pi\frac{\pi^{N-1}}{\Gamma(N)}\sin^{2(N-1)}(\phi),\\ &= \frac{2\,\pi^N}{\Gamma(N)}\left(1-w^2\right)^{N-1}.\end{aligned} \tag{13}$$

Dividing (13) by the surface $\frac{2\,\pi^N}{\Gamma(N)}$ of $\mathbb{S}^{2N-1}$ leads to the expected result (5). This geometrical approach provides an alternative to the traditional one based on statistical tools [1].

D. Extending Hotelling's Approach to the GLRT

Unfortunately, Hotelling's result is not immediately applicable to the considered GLRT (12): since a maximization on the parameter θ is introduced, the surface of interest is spread around a 2D manifold as will be seen now.

The acceptance region in this case is a new tube $\mathcal{T}_{\text{off-grid}}$ around the two-dimensional manifold $\boldsymbol{\gamma}(\theta,\alpha)$:

$$\mathcal{T}_{\text{off-grid}} = \left\{\underline{\mathbf{u}} \in \mathbb{S}^{2N-1} : \max_{\theta\in\mathcal{D},\alpha} \boldsymbol{\gamma}(\theta,\alpha)^T \underline{\mathbf{u}} > w\right\}.$$

Note that in this case, $\mathcal{T}_{\text{off-grid}}$ follows a manifold that is often not closed since, writing $\mathcal{D} = [\theta_1,\theta_2]$, $\boldsymbol{\gamma}(\theta_1,\alpha) \neq \boldsymbol{\gamma}(\theta_2,\alpha)$ in general. Unlike previously, when computing the surface of the tube, a term accounting for its boundaries will appear.

Hotelling's result does not cover this multi-dimensional manifold case as it gives the surface of a tube around a curve. However, in [31] and [39], this result is extended to a special case of two-dimensional manifolds embedded on $\mathbb{S}^{n-1}$ which is of interest to us:

Theorem III.2: [31] For $i \in [1,2]$, let $\boldsymbol{\gamma}_i : [\theta_1,\theta_2] \to \mathbb{S}^{n-1}$ be regular curves. Assume $\boldsymbol{\gamma}_1(\theta)^T\boldsymbol{\gamma}_2(\theta) = 0$ for all θ. Let $Z(\theta) = \left[\left(\boldsymbol{\gamma}_1(\theta)^T\underline{\mathbf{u}}\right)^2 + \left(\boldsymbol{\gamma}_2(\theta)^T\underline{\mathbf{u}}\right)^2\right]^{1/2}$ where $\underline{\mathbf{u}}$ is uniformly distributed on $\mathbb{S}^{n-1}$. Then for $0 < w < 1$, we have, under no overlap regime, i.e. low P_{FA} regimes (see Section IV for a detailed study):

$$\begin{aligned}\mathbb{P}\left(\max_{\theta_1\le\theta\le\theta_2} Z(\theta) > w\right) &= \left(1-w^2\right)^{(n-2)/2}\\ &+ \frac{\Gamma\left(\frac{n}{2}\right)\, w\left(1-w^2\right)^{(n-3)/2}}{2\pi^{3/2}\,\Gamma\left(\frac{n-1}{2}\right)}\\ &\times \int_{\theta_1}^{\theta_2}\int_0^{2\pi}\Big[\left\|\dot{\boldsymbol{\gamma}}_1(\theta)\cos\Omega + \dot{\boldsymbol{\gamma}}_2(\theta)\sin\Omega\right\|^2\\ &\qquad -\left(\dot{\boldsymbol{\gamma}}_1(\theta)^T\boldsymbol{\gamma}_2(\theta)\right)^2\Big]^{1/2} d\Omega\, d\theta\,,\end{aligned} \tag{14}$$

where $\dot{\boldsymbol{\gamma}}_i(\theta)$ is the derivative of $\boldsymbol{\gamma}_i(\theta)$ with respect to θ. When there is overlap, i.e., high P_{FA} regimes, the right-hand side of (14) becomes an upper bound.

It turns out that we can reformulate our problem to fulfill the assumptions of the above theorem with $n = 2N$. Indeed, using (10) and (11), we can check that:

$$\left|\mathbf{s}\left(\theta\right)^H \mathbf{u}\right|^2 = \left|\boldsymbol{\gamma}_1(\theta)^T \underline{\mathbf{u}}\right|^2 + \left|\boldsymbol{\gamma}_2(\theta)^T \underline{\mathbf{u}}\right|^2,$$

so that Theorem III.2 gives us the desired P_{FA} (when equality holds in (14)). Follows our result:

Corollary III.2.1: In the absence of overlap (low P_{FA} regimes), the P_{FA} for the GLRT (7) for a search interval $\mathcal{D} = [\theta_1, \theta_2]$ with the steering vector $\mathbf{d}\left(\theta\right)$ defined in (1) is given by:

$$P_{FA} = (1-w^2)^{N-1} + \frac{\Gamma(N)\, w\, (1-w^2)^{N-\frac{3}{2}}}{\pi^{1/2}\Gamma\left(N-\frac{1}{2}\right)} \int_{\theta_1}^{\theta_2} \left\|\dot{\boldsymbol{\gamma}}_1(\theta)^T \mathbf{P}^{\perp}_{\boldsymbol{\gamma}_2(\theta)}\right\| d\theta. \tag{15}$$

where $\mathbf{P}^{\perp}_{\boldsymbol{\gamma}_2(\theta)} = \mathbf{I} - \boldsymbol{\gamma}_2(\theta)\boldsymbol{\gamma}_2(\theta)^T$ is the orthogonal projector on $\boldsymbol{\gamma}_2(\theta)$. Under white noise ($\boldsymbol{\Gamma} = \sigma^2\,\mathbf{I}$), this result simplifies to:

$$P_{FA} = (1-w^2)^{N-1} + \sqrt{\frac{\pi}{3}}\, \frac{\Gamma(N)\, w\, (1-w^2)^{N-\frac{3}{2}}}{\Gamma\left(N-\frac{1}{2}\right)}\, \left(N^2-1\right)^{\frac{1}{2}}\, (\theta_2 - \theta_1). \tag{16}$$

When $\mathcal{D} = [0, 1]$, the first term has to be removed from the equations.

The integral in (15) can be easily evaluated numerically.

Proof: First, notice that the derivatives $\dot{\boldsymbol{\gamma}}_1(\theta)$ and $\dot{\boldsymbol{\gamma}}_2(\theta)$ are orthogonal, and that $\|\dot{\boldsymbol{\gamma}}_1(\theta)\| = \|\dot{\boldsymbol{\gamma}}_2(\theta)\|$. Thus, for all $\Omega \in [0, 2\pi]$, we have that

$$\left\|\dot{\boldsymbol{\gamma}}_1(\theta)\cos\Omega + \dot{\boldsymbol{\gamma}}_2(\theta)\sin\Omega\right\|^2 = \left\|\dot{\boldsymbol{\gamma}}_1(\theta)\right\|^2,$$

which does not depend on Ω. The double integral simplifies:

$$\begin{aligned}
&\int_{\theta_1}^{\theta_2}\int_0^{2\pi} \Big[\left\|\dot{\boldsymbol{\gamma}}_1(\theta)\cos\Omega + \dot{\boldsymbol{\gamma}}_2(\theta)\sin\Omega\right\|^2 \\
&\qquad - \left(\dot{\boldsymbol{\gamma}}_1(\theta)^T\boldsymbol{\gamma}_2(\theta)\right)^2\Big]^{1/2} d\Omega\, d\theta, \\
&= 2\pi \int_{\theta_2}^{\theta_1} \left[\left\|\dot{\boldsymbol{\gamma}}_1(\theta)\right\|^2 - \left(\dot{\boldsymbol{\gamma}}_1(\theta)^T\boldsymbol{\gamma}_2(\theta)\right)^2\right]^{1/2} d\theta, \\
&= 2\pi \int_{\theta_1}^{\theta_2} \left\|\dot{\boldsymbol{\gamma}}_1(\theta)^T \mathbf{P}^{\perp}_{\boldsymbol{\gamma}_2(\theta)}\right\| d\theta,
\end{aligned} \tag{17}$$

In the case of white noise, this integral can be computed analytically. Let $\mathbf{x}$ be the following vector:

$$\mathbf{x} = 2\pi\, [0, 1, \ldots, N-1]^T,$$

so that

$$\dot{\boldsymbol{\gamma}}_1(\theta) = \begin{bmatrix}\mathbf{x}\\ \mathbf{x}\end{bmatrix} \odot \boldsymbol{\gamma}_2(\theta), \tag{18}$$

$$\dot{\boldsymbol{\gamma}}_2(\theta) = -\begin{bmatrix}\mathbf{x}\\ \mathbf{x}\end{bmatrix} \odot \boldsymbol{\gamma}_1(\theta). \tag{19}$$

Then:

$$\left\|\dot{\boldsymbol{\gamma}}_1(\theta)\right\| = \left\|\dot{\boldsymbol{\gamma}}_2(\theta)\right\| = 2\pi\sqrt{\frac{(N-1)(2N-1)}{6}}. \tag{20}$$

and

$$\begin{aligned}
\dot{\boldsymbol{\gamma}}_1(\theta)^T\boldsymbol{\gamma}_2(\theta) &= \left(\begin{bmatrix}\mathbf{x}\\ \mathbf{x}\end{bmatrix} \odot \boldsymbol{\gamma}_2(\theta)\right)^T \boldsymbol{\gamma}_2(\theta), \\
&= \frac{2\pi}{N}\sum_{k=0}^{N-1} k = \pi\,(N-1).
\end{aligned} \tag{21}$$

Then, injecting (20) and (21) into (17):

$$2\pi \int_{\theta_1}^{\theta_2} \left\|\dot{\boldsymbol{\gamma}}_1(\theta)^T \mathbf{P}^{\perp}_{\boldsymbol{\gamma}_2(\theta)}\right\| d\theta = 2(\theta_2-\theta_1)\pi^2\sqrt{\frac{(N^2-1)}{3}}. \tag{22}$$

Replacing the double integral in (14) with (22) gives the expected result. ■

Interestingly, note that the first term in (16) represents the surface of the two semi-spherical caps at the extremities of the tube. As such, it equals the P_{FA} of the NMF expressed in (5). The second term shows the influence of the manifold induced by the off-grid nature of the problem. It is analogous to the one-dimensional case of Theorem III.1, divided by the surface of $\mathbb{S}^{2N-1}$. Here, $\theta_2 - \theta_1$ plays the role of the manifold length, and the rest of the rightmost term is the surface of the cross-section divided by the area of $\mathbb{S}^{2N-1}$. When $\mathcal{D} = [0, 1]$, the ends of the tube meet, and the end semi-spherical caps vanish into the main component: this can be visualized as if going from Fig. 2 to Fig. 3. This explains why the first term should be removed when $\mathcal{D} = [0, 1]$: it is already included in the second term.

One point of interest that can be seen looking at formula (15) is that the off-grid NMF (7) is not CFAR with respect neither to $\boldsymbol{\Gamma}$ or $\mathcal{D}$. This is explained by the fact that the length of the whitened manifold $\mathbf{s}(\theta)$ varies with both $\boldsymbol{\Gamma}$ and $\mathcal{D}$. As a result, the surface of the tube around this manifold also varies, and thus so does the P_{FA}. To the best of our knowledge, this result is not discussed in the current literature.

The relationships in Corollary III.2.1 are upper bounds in the presence of overlap. In this case, they still hold interest in the radar context where controlling the P_{FA} is fundamental. The following section investigates the conditions under which no overlap happens.

IV. On the Appearance of Overlap

The goal of this section is to determine for which thresholds formula (14) (formula (16) in the case of white noise) holds equality. This requires us to investigate the conditions under which overlap occurs. We will start by exhibiting general results from [33], [34] and some original results on shift-invariant manifolds before delving into our specific problem.

Let us consider an M-dimensional manifold $\mathcal{M} = \{\boldsymbol{\gamma}(\boldsymbol{\xi}), \boldsymbol{\xi} = (\xi_1, \ldots, \xi_M) \in \mathcal{D}\}$ defined on the search domain $\mathcal{D}$ over $\mathbb{S}^{n-1}$ and let us consider the tube $\mathcal{T}$ over $\mathbb{S}^{n-1}$ around $\mathcal{M}$ consisting of the points $\mathbf{u}$ satisfying $\mathbf{u}^T\boldsymbol{\gamma}(\boldsymbol{\xi}) > w$ for some $\boldsymbol{\xi}$ in $\mathcal{D}$. $\mathcal{M}$ can be seen, loosely speaking, as the axis of $\mathcal{T}$. The cross-section $\mathcal{CS}_{\boldsymbol{\xi}}$ defined in [33] at a point $\boldsymbol{\xi}$ belonging to $\mathcal{M}$ is the set of points of $\mathcal{T}$ orthogonal to the derivatives of $\boldsymbol{\gamma}$ in $\boldsymbol{\xi}$. Formally:

$$\mathcal{CS}_{\boldsymbol{\xi}} = \left\{\mathbf{u} \in \mathcal{T}, \mathbf{u}^T \frac{\partial \boldsymbol{\gamma}}{\partial \boldsymbol{\xi}^T} = \mathbf{0}, \mathbf{u}^T\boldsymbol{\gamma}(\boldsymbol{\xi}) > w\right\}. \tag{23}$$

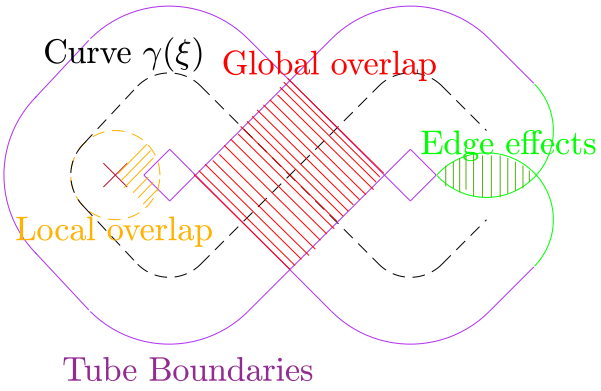

Fig. 4. Illustration of all the phenomena leading to an overestimation of the P_{FA} when using (16).

Excluding the edge effects defined later in this section, the tube defined as the union of cross-sections overlaps if and only if a point $\mathbf{u}$ of $\mathcal{T}$ belongs to more than one cross-section: in this case, Hotelling's geometrical approach and its extensions lead to an overestimation of the Probability of False Alarm. Otherwise, the equality holds in (14). Two types of overlap are defined in [30]: local overlap, which derives from local differential properties of the manifold generating the tube, and non-local overlap, which depends on the overall shape of the tube. Global overlap encompasses both types of overlap. It is linked to a limit overlap threshold w_{lim} and there is no overlap if:

$$w \geq w_{\text{lim}}\,. \tag{24}$$

The limit threshold can be equivalently seen as an angle ϕ_{lim} such that

$$\cos\phi_{\text{lim}} = w_{\text{lim}}\,,$$

and there is no overlap if

$$\phi = \cos^{-1} w \leq \phi_{\text{lim}}\,.$$

In the sequel, the conditions are expressed in terms of ϕ_{lim}.

In addition to those phenomena, edge effects also have to be considered. They can appear when dealing with non-closed manifold and cause the same problems as overlap i.e. an overestimation of the P_{FA}. In the 1D case illustrated in Fig. 2, edge effects would occur when the green semi-spherical caps at the end overlap. A manifold is said to be closed along dimension k if its k-th variable ξ_k belongs to an interval $[\xi_{k_1}, \xi_{k_2}]$ such that $\boldsymbol{\gamma}(\xi_1,\ldots,\xi_{k_1},\ldots,\xi_M) = \boldsymbol{\gamma}(\xi_1,\ldots,\xi_{k_2},\ldots,\xi_M)$ for all $\xi_i, i \neq k$. A manifold is said to be closed if it is closed along all its dimensions.

Fig. 4 summarizes all the phenomena that can arise.

A. The General Case

In this section, we give the conditions under which no overlap happens under general conditions for any M-dimensional manifold $\boldsymbol{\gamma}(\xi_1,\ldots,\xi_M)$ embedded in $\mathbb{S}^{n-1}$.

In [33], a criterion for characterizing the overlap of a tube embedded on a sphere around a curve is introduced that is a direct consequence of the fact that the union of the cross-section needs to be disjoint. It turns out that the arguments used by the authors can be generalized to find overlap criteria for tubes around any M-dimensional manifolds, as suggested in [34].

Theorem IV.1: [33], [34] Let $\boldsymbol{\gamma}(\boldsymbol{\xi})$ be a $C^2 M$-dimensional manifold parameterized by $\boldsymbol{\xi} = (\xi_1,\ldots,\xi_M) \in \mathcal{D}$. Let ϕ_{lim} be the limit angle for which no overlap occurs, related to w_{lim} (24) by $\cos(\phi_{\text{lim}}) = w_{\text{lim}}$. Let $\mathbf{P}_{\boldsymbol{\xi}'}$ be the projection onto the subspace spanned by $\boldsymbol{\gamma}(\boldsymbol{\xi}')$ and its derivatives $\dfrac{\partial\boldsymbol{\gamma}}{\partial\boldsymbol{\xi}'}$. ϕ_{lim} is given by:

$$\begin{aligned}\cot^2\phi_{\text{lim}} &= \sup_{\boldsymbol{\xi},\boldsymbol{\xi}'\in\mathcal{D}^2} \frac{1-\boldsymbol{\gamma}(\boldsymbol{\xi})^T\mathbf{P}_{\boldsymbol{\xi}'}\boldsymbol{\gamma}(\boldsymbol{\xi})}{\left(1-\boldsymbol{\gamma}(\boldsymbol{\xi})^T\boldsymbol{\gamma}(\boldsymbol{\xi}')\right)^2},\\ &\triangleq \sup_{\boldsymbol{\xi},\boldsymbol{\xi}'\in\mathcal{D}^2} h(\boldsymbol{\xi},\boldsymbol{\xi}').\end{aligned} \tag{25}$$

The criterion (25) encompasses both local and non-local overlap:

$$\phi_{\text{lim}} = \min\{\phi_{\text{local}}, \phi_{\text{non-local}}\}\,, \tag{26}$$

where ϕ_{local} and $\phi_{\text{non-local}}$ are the limit angles such that local and non-local overlaps occur. Local overlap occurs when $\boldsymbol{\xi}'$ tends to $\boldsymbol{\xi}$, and non-local overlap arises when the sup of h in (25) is attained for $\boldsymbol{\xi} \neq \boldsymbol{\xi}'$. Note that (25) does not consider edge effects.

It can be simplified in the case of a shift-invariant manifold:

Definition IV.1: A real manifold $\boldsymbol{\gamma}(\boldsymbol{\xi})$ is said to be shift-invariant when, for any $\boldsymbol{\xi},\boldsymbol{\xi}'$, the scalar product $\boldsymbol{\gamma}(\boldsymbol{\xi})^T\boldsymbol{\gamma}(\boldsymbol{\xi}')$ depends only on $\boldsymbol{\xi}-\boldsymbol{\xi}'$:

$$\boldsymbol{\gamma}(\boldsymbol{\xi})^T\boldsymbol{\gamma}(\boldsymbol{\xi}') = f(\boldsymbol{\xi}-\boldsymbol{\xi}'),$$

where f is an even function.

Then, similarly to the case of a single parameter, we have the following property:

Proposition IV.1: For a shift-invariant manifold $\boldsymbol{\gamma}(\boldsymbol{\xi})$, h as defined in (25) is a function of $\boldsymbol{\xi}-\boldsymbol{\xi}'$: $h(\boldsymbol{\xi},\boldsymbol{\xi}') = g(\boldsymbol{\xi}-\boldsymbol{\xi}')$. Consequently,

$$\cot^2\phi_{\text{lim}} = \sup_{\mathbf{x}\in\mathcal{E}} g(\mathbf{x}), \tag{27}$$

where $\mathcal{E}$ is the image of $\mathcal{D}\times\mathcal{D}$ by the function $(\boldsymbol{\xi},\boldsymbol{\xi}') \to \boldsymbol{\xi}-\boldsymbol{\xi}'$.

Proof: The proof is given in Appendix B. ■

The implications of this result are detailed in the following sections.

1) On Local Overlap: In this section, we discuss the occurrence of local overlap around a M-dimensional manifold. The results of this section are particularized to our complex signal model (1) in Section IV-B1.

Local overlap is linked to the curvature of the manifold. To illustrate this, consider the case of a tube around a curve in Euclidean space drawn in Fig. 5: there is local overlap whenever the tube radius is greater than the radius of curvature of the curve.

A local overlap criterion is developed in [34, Annex A.2]. Recall that it corresponds to the case where $\boldsymbol{\xi}'$ tends to $\boldsymbol{\xi}$.

We define the local overlap angle ϕ_{local} in $\boldsymbol{\xi}$ similarly in the multi-dimensional case as:

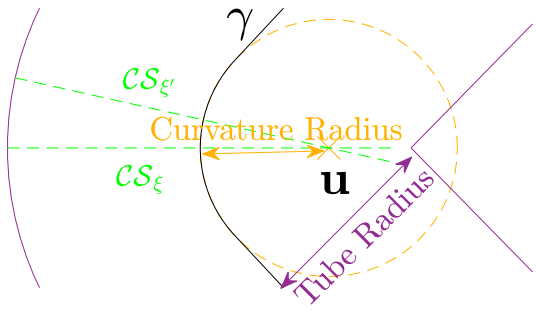

Fig. 5. Illustration of local overlap in 1D in the Euclidean case. Here, the radius of the tube (in red) is greater than the radius of curvature. This causes overlap: see, for example, that the point $\mathbf{u}$ belongs to both cross-sections $\mathcal{CS}_{\xi}$ and $\mathcal{CS}_{\xi'}$.

Corollary IV.1.1: [34, Annex A.2] In the case of a tube around an M-dimensional manifold $\boldsymbol{\gamma}$, using the same notations as before with $\boldsymbol{\beta}$ representing the directions of convergence from $\boldsymbol{\xi}'$ to $\boldsymbol{\xi}$, the limit local overlap angle is given by:

$$\begin{aligned}\cot^2 \phi_{\text{local}} &= \sup_{\boldsymbol{\xi}\in\mathcal{D}} \sup_{\boldsymbol{\beta}\in\mathbb{S}^{M-1}} \lim_{\epsilon\to 0} h(\boldsymbol{\xi}, \boldsymbol{\xi} + \epsilon\,\boldsymbol{\beta}),\\ &= \sup_{\boldsymbol{\xi}\in\mathcal{D}} \sup_{\boldsymbol{\beta}\in\mathbb{S}^{M-1}} \frac{\left\| \sum_{i,j} \beta_i\beta_j \left(\mathbf{I} - \mathbf{P}_{\boldsymbol{\xi}}\right) \frac{\partial^2\boldsymbol{\gamma}}{\partial\xi_i\,\partial\xi_j} \right\|^2}{\left(\sum_{i,j} \beta_i\beta_j \frac{\partial\boldsymbol{\gamma}^T}{\partial\xi_i} \frac{\partial\boldsymbol{\gamma}}{\partial\xi_j} \right)^2}.\end{aligned} \tag{28}$$

Readers can refer to [34, Annex A.2] for an interpretation in terms of principal curvatures.

Proof: The proof is given in [34, Annex A.2]. ■

The formula (28) can be simplified in the case of a shift-invariant manifold: (27) shows that the maximization on $\boldsymbol{\xi}$ can be dropped in (28). Indeed, $h(\boldsymbol{\xi}, \boldsymbol{\xi}')$ only depends on the difference $\boldsymbol{\xi} - \boldsymbol{\xi}'$. The following developments allow us to go further:

Corollary IV.1.2: Let $\boldsymbol{\gamma}(\boldsymbol{\xi})$ be a M-dimensional shift-invariant manifold, and let $\mathbf{G}$ be its first fundamental form:

$$\mathbf{G} = \frac{\partial\boldsymbol{\gamma}}{\partial\boldsymbol{\xi}}^T \frac{\partial\boldsymbol{\gamma}}{\partial\boldsymbol{\xi}}\,. \tag{29}$$

Then $\mathbf{G}$ does not depend on ξ. Besides, let

$$\mathbf{G} = \mathbf{G}^{T/2}\,\mathbf{G}^{1/2}\,, \tag{30}$$

and $\boldsymbol{\mu}$ be a reparametrization of $\boldsymbol{\gamma}$ defined by

$$\boldsymbol{\mu} = \mathbf{G}^{1/2}\,\boldsymbol{\xi}\,, \tag{31}$$

Then

$$\frac{\partial\boldsymbol{\gamma}^T}{\partial\mu_i} \frac{\partial\boldsymbol{\gamma}}{\partial\mu_j} = \delta_{ij}\,, \tag{32}$$

and (28) reduces to:

$$\cot\phi^2_{\text{local}} = \sup_{\boldsymbol{\beta}\in\mathbb{S}^{M-1}} \left\| \sum_{i,j} \beta_i\beta_j \left(\frac{\partial^2\boldsymbol{\gamma}}{\partial\mu_i\partial\mu_j} \right) \right\|^2 - 1\,. \tag{33}$$

Proof: The proof is given in the Appendix C. ■

2) On Non-Local Overlap: Non-local overlap arises when the tube draws back into itself, as shown in blue in Fig. 4 for a tube spanned by a curve. In [33], it is shown in the case $M = 1$ that the limit angle around a closed manifold $\boldsymbol{\gamma}(\boldsymbol{\xi})$ linked to this type of overlap can be characterized entirely by looking at the pairs of points $(\boldsymbol{\xi}, \boldsymbol{\xi}')$ that minimize locally the distance $\left\|\boldsymbol{\gamma}(\boldsymbol{\xi}) - \boldsymbol{\gamma}(\boldsymbol{\xi}')\right\|$, with $\boldsymbol{\xi} \neq \boldsymbol{\xi}'$. In such case, (25) reduces to an intuitive geodesic distance criteria when $\boldsymbol{\xi} \neq \boldsymbol{\xi}'$. In the general case, M is arbitrary, and the following holds:

Proposition IV.2: Consider a tube around the M-dimensional manifold $\boldsymbol{\gamma}$ lying on the sphere. The set of pairs $(\boldsymbol{\xi}, \boldsymbol{\xi}')$ that characterizes non-local overlap is:

$$\begin{aligned}\Xi = \Big\{ (\boldsymbol{\xi}, \boldsymbol{\xi}') : \boldsymbol{\xi} \neq \boldsymbol{\xi}', \left(\boldsymbol{\gamma}(\boldsymbol{\xi}) - \boldsymbol{\gamma}(\boldsymbol{\xi}')\right)^T \frac{\partial\boldsymbol{\gamma}}{\partial\xi_k} = 0\\ \text{and } \left(\boldsymbol{\gamma}(\boldsymbol{\xi}) - \boldsymbol{\gamma}(\boldsymbol{\xi}')\right)^T \frac{\partial\boldsymbol{\gamma}}{\partial\xi'_k} = 0,\ \forall k \in [1, M] \Big\}.\end{aligned} \tag{34}$$

Then, if the manifold is closed:

$$\phi_{\text{non-local}} = \min_{(\boldsymbol{\xi},\boldsymbol{\xi}')\in\Xi} \frac{1}{2} \cos^{-1}\left(\boldsymbol{\gamma}(\boldsymbol{\xi})^T \boldsymbol{\gamma}(\boldsymbol{\xi}')\right). \tag{35}$$

For a non-closed manifold, a term accounting for the boundaries must be taken into account:

$$\phi_{\text{non-local}} = \min\left\{ \min_{(\boldsymbol{\xi},\boldsymbol{\xi}')\in\Xi} \frac{1}{2} \cos^{-1}\left(\boldsymbol{\gamma}(\boldsymbol{\xi})^T \boldsymbol{\gamma}(\boldsymbol{\xi}')\right), E \right\}, \tag{36}$$

where

$$E = \inf_{(\boldsymbol{\xi},\boldsymbol{\xi}')\in\mathcal{B}\times\mathcal{D}} \cot^{-1}\sqrt{h\left(\boldsymbol{\xi}, \boldsymbol{\xi}'\right)}\,. \tag{37}$$

Proof: It is possible to adapt the proof of Proposition 4.2 of [33] for an M-dimensional manifold using the principal curvature interpretation of (28) and by considering frontiers around the local minima. The extension to the case of a non-closed manifold is then straightforward. ■

In the non-closed case, the limit angle $\phi_{\text{non-local}}$ also encompasses instances of local overlap when ξ' tends to $\xi \in \mathcal{B}$. Plugging it in (26) still yields the right exact limit angle ϕ_{lim}.

As noted in [33], this formulation is not necessarily more straightforward to use than (25) since it can be more involved to find the set of pairs Ξ than to compute (25). However, in Section IV-B2, we show that, in our specific case, it enables us to reduce the computational complexity of the search dramatically.

3) On Edge Effects: The formula (25) does not consider edge effects that can arise when dealing with non-closed manifolds. Indeed, noting $\mathcal{B}$ the boundaries of $\mathcal{D}$, (25) is defined for $\boldsymbol{\xi} \in \mathcal{D}$, $\boldsymbol{\xi}' \in \mathcal{D} \setminus \mathcal{B}$. Edge effects appear when a point $\mathbf{u}$ is such that there exist two distinct points $\boldsymbol{\xi}_1$, $\boldsymbol{\xi}_2$ in $\mathcal{B}$ such that $\mathbf{u}^T\boldsymbol{\gamma}(\boldsymbol{\xi}_1) > w$ and $\mathbf{u}^T\boldsymbol{\gamma}(\boldsymbol{\xi}_2) > w$. It is illustrated in Fig. 4 in the case $M = 1$. One has to check that the limit angle ϕ_{lim} is big enough so that edge effects do not appear.

B. Application to the Complex Signal Model (1)

We apply here the general results of the previous section to our case of interest where $\boldsymbol{\gamma}$ is given by (10), defined on $\mathcal{D} \times [0, 2\pi]$. This first result gives the limit global overlap threshold for our application:

Corollary IV.1.3: With $\boldsymbol{\gamma}$ defined as in (10), the limit angle for no global overlap is:

$$\cot^2 \phi_{\text{lim}} = \sup_{\substack{\theta,\alpha\in\mathcal{D}\times[0,2\pi] \\ \theta',\alpha'\in\mathcal{D}\times[0,2\pi]}} \frac{1-\boldsymbol{\gamma}(\theta,\alpha)^T \mathbf{P}_{\theta',\alpha'} \boldsymbol{\gamma}(\theta,\alpha)}{\left(1-\boldsymbol{\gamma}(\theta,\alpha)^T\boldsymbol{\gamma}(\theta',\alpha')\right)^2}, \quad (38)$$

where $\mathbf{P}_{\theta',\alpha'} = \mathbf{I} - \mathbf{P}^{\perp}_{\theta',\alpha'}$ with $\mathbf{P}^{\perp}_{\theta',\alpha'}$ defined later in (41).

Proof: We simply inject (10) in (25). ■

Under white noise, for one cell $\mathcal{D}_k$, one can check numerically that the corresponding limit P_{FA} is equal to:

$$P_{FA\,\text{lim}} \approx 10^{-2.52}, \quad (39)$$

Fortunately, this P_{FA} is well above the common P_{FA} encountered in radar applications.

In the following sections, we discuss how to find the limit angles ϕ_{local} and $\phi_{\text{non-local}}$. Indeed, the search domain in (38) is 4-dimensional, so the criterion can be heavy to evaluate. We can accelerate the search of the global limit angle by first finding the local and non-local overlap angle ϕ_{local} and $\phi_{\text{non-local}}$ through (28) and (35) then combining them using (26).

1) On Local Overlap: The following corollary gives ϕ_{local} in our case:

Corollary IV.1.4: For our manifold $\boldsymbol{\gamma}$ defined in (10), we have:

$$\cot^2 \phi_{\text{local}} = \sup_{\theta,\alpha\in\mathcal{D}\times[0,2\pi]} \sup_{\varphi\in[0,2\pi]} J(\theta,\alpha,\varphi), \quad (40)$$

where

$$J(\theta,\alpha,\varphi) = \frac{\left\| \mathbf{P}^{\perp}_{\theta,\alpha}\left(\cos^2\varphi \frac{\partial^2\boldsymbol{\gamma}}{\partial\theta^2} + \sin 2\varphi \frac{\partial^2\boldsymbol{\gamma}}{\partial\theta\partial\alpha} + \sin^2\varphi \frac{\partial^2\boldsymbol{\gamma}}{\partial\alpha^2}\right)\right\|}{\cos^2\varphi \left\|\frac{\partial\boldsymbol{\gamma}}{\partial\theta}\right\|^2 + \sin 2\varphi \frac{\partial\boldsymbol{\gamma}^T}{\partial\theta}\frac{\partial\boldsymbol{\gamma}}{\partial\alpha} + \sin^2\varphi \left\|\frac{\partial\boldsymbol{\gamma}}{\partial\alpha}\right\|^2},$$

and

$$\mathbf{P}^{\perp}_{\theta,\alpha} = \mathbf{I} - \mathbf{M}_{\theta,\alpha}\left(\mathbf{M}^T_{\theta,\alpha}\mathbf{M}_{\theta,\alpha}\right)^{-1}\mathbf{M}^T_{\theta,\alpha}, \quad (41)$$

with $\mathbf{M}_{\theta,\alpha} = \left[\boldsymbol{\gamma}(\theta,\alpha), \frac{\partial\boldsymbol{\gamma}(\theta,\alpha)}{\partial\theta}, \frac{\partial\boldsymbol{\gamma}(\theta,\alpha)}{\partial\alpha}\right]$. This expression can be easily evaluated setting $\boldsymbol{\beta} = [\cos(\varphi), \sin(\varphi)]$ and then maximizing on φ.

Proof: We simply inject (10) in (28), with $M = 2$. ■

The derivatives of $\boldsymbol{\gamma}$ are found from a straightforward derivation using (18) and (19):

$$\frac{\partial\boldsymbol{\gamma}}{\partial\theta} = \left(\mathbf{I} - \boldsymbol{\gamma}(\theta,\alpha)\boldsymbol{\gamma}(\theta,\alpha)^H\right) \times \left(\cos\alpha\,\boldsymbol{\gamma}_2(\theta) - \sin\alpha\,\boldsymbol{\gamma}_1(\theta)\right) \odot \begin{bmatrix}\mathbf{x}\\ \mathbf{x}\end{bmatrix},$$

$$\frac{\partial\boldsymbol{\gamma}}{\partial\alpha} = -\sin\alpha\,\boldsymbol{\gamma}_1(\theta) + \cos\alpha\,\boldsymbol{\gamma}_2(\theta).$$

It is possible to find the analytical limit threshold for local overlap under white noise.

Corollary IV.1.5: Under white noise with the signal model as in (1), the limit local angle (40) is:

$$\phi_{\text{local}} = \tan^{-1}\left(\frac{\sqrt{5-C}}{2}\right),$$

and the limit local threshold is

$$w^2_{\text{local}} = \cos^2\left(\tan^{-1}\left(\frac{\sqrt{5-C}}{2}\right)\right), \quad (42)$$

where

$$C = \frac{3}{5}\frac{3N^2-7}{(N-1)^2}. \quad (43)$$

Proof: The proof is given in Appendix D. ■

Note that $\lim_{N\to\infty} C = \frac{9}{5}$: for N large enough,

$$w^2_{\text{local}} \approx \cos^2\left(\tan^{-1}\left(\frac{2}{\sqrt{5}}\right)\right). \quad (44)$$

For $N = 10$, according to (16) this corresponds to the limit:

$$P_{FA\,\text{local}} \approx 10^{-2.52} = P_{FA\,\text{lim}}.$$

thus local overlap is the limiting factor for the white noise setting.

2) On Non-Local Overlap: First, consider the case where the target is searched over the whole spectral domain i.e. $\mathcal{D} = [0,1]$. This corresponds to the operational context where a single target is searched in the scene. In this case, the manifold $\boldsymbol{\gamma}$ in (10) is closed. In order to compute the non-local limit angle $\phi_{\text{non-local}}$, one should evaluate criterion (35). The following corollary simplifies the criteria.

Corollary IV.1.6: Consider a tube lying on the sphere around the manifold $\boldsymbol{\gamma}$ defined in (10). Define Ξ' as:

$$\Xi' = \left\{(\theta,\theta') : \theta \neq \theta', \frac{\partial\left|\mathbf{s}(\theta)^H\mathbf{s}(\theta')\right|}{\partial\theta} = 0\right\}. \quad (45)$$

Then when $\mathcal{D} = [0,1]$, $\phi_{\text{non-local}}$ in (35) reduces to:

$$\phi_{\text{non-local}} = \min_{(\theta,\theta')\in\Xi'} \frac{1}{2}\cos^{-1}\left|\mathbf{s}(\theta)^H\mathbf{s}(\theta')\right|. \quad (46)$$

and otherwise, when $\mathcal{D} = [\theta_1,\theta_2] \subsetneq [0,1]$, $\phi_{\text{non-local}}$ in (36) reduces to

$$\phi_{\text{non-local}} = \min\left\{\min_{(\theta,\theta')\in\Xi'} \frac{1}{2}\cos^{-1}\left|\mathbf{s}(\theta)^H\mathbf{s}(\theta')\right|, E\right\}. \quad (47)$$

where E has been defined in (37), with $\mathcal{B} = \{\theta_1,\theta_2\}\times[0,2\pi]$ and $\boldsymbol{\xi} = (\theta,\alpha)$, $\boldsymbol{\xi}' = (\theta',\alpha')$.

Proof: The proof is provided in Appendix E. ■

This simplif ication allows us to investigate the critical points with $(\theta \neq \theta')$ of ambiguity maps $\left|\mathbf{s}(\theta)^H\mathbf{s}(\theta')\right|$ such as the examples drawn on Fig. 6. In the case of a closed manifold, i.e., $\mathcal{D} = [0,1]$, the search procedure (46) becomes two-dimensional. When $\mathcal{D} = [\theta_1,\theta_2] \subsetneq [0,1]$, one has to evaluate (37) in order to compute (47). The search procedure (47) is thus three-dimensional. Under white noise, $\boldsymbol{\gamma}$ is shift-invariant. The search space can be further simplified and is of dimension 1: indeed, in this case, the product $\left|\mathbf{s}(\theta)^H\mathbf{s}(\theta')\right|$ depends only on the difference $\delta = \theta' - \theta$. Finding the local maxima of $\left|\mathbf{s}(\theta)^H\mathbf{s}(\theta')\right|$ simply reduces in finding the local maxima of

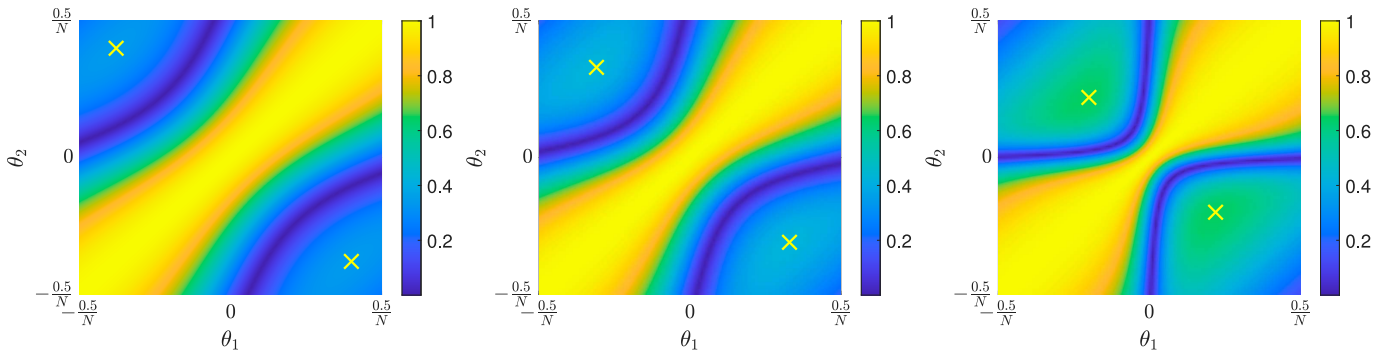

(a) $\rho = 0.9$. (b) $\rho = 0.95$. (c) $\rho = 0.99$.

Fig. 6. Examples of ambiguity maps $\left|\mathbf{s}(\theta)^H \mathbf{s}(\theta')\right|$ drawn for $\theta, \theta' \in \mathcal{D}_0$ for highly correlated noise (see Eq. (52) for the definition of ρ), with $N = 10$. Crosses represent local maxima.

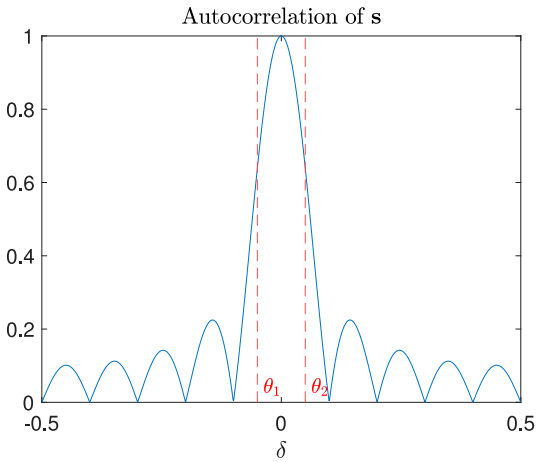

Fig. 7. Autocorrelation of $\mathbf{s}$ under white noise (48) for $N = 10$. Values θ_1, θ_2 represent the limits of a cell $\mathcal{D}_k = [\theta_1, \theta_2]$.

$\left|\mathbf{s}(\theta)^H \mathbf{s}(\theta + \delta)\right|$ for any fixed θ. $\left|\mathbf{s}(\theta)^H \mathbf{s}(\theta + \delta)\right|$ represents the autocorrelation of $\mathbf{s}$, and it is well known that:

$$\left|\mathbf{s}(\theta)^H \mathbf{s}(\theta + \delta)\right| = \frac{1}{N} \left| \frac{\sin(\pi \delta N)}{\sin(\pi \delta)} \right| . \tag{48}$$

The autocorrelation of $\mathbf{s}$ is represented in Fig. 7. In this case, in a single cell $\mathcal{D}_k$ the set Ξ' is empty since the derivative of $\left|\mathbf{s}(\theta)^H \mathbf{s}(\theta + \delta)\right|$ only vanishes for $\delta = 0$. If $\mathcal{D} = [0, 1]$, $\phi_{\text{non-local}}$ can be readily obtained from the first secondary lobe.

C. On Edge Effects

If $\mathcal{D} = [\theta_1, \theta_2] \subsetneq [0, 1]$, then $\mathcal{B} = \{\theta_1, \theta_2\} \times [0, 2\pi]$ and one has to take into account edge effects. The result in Appendix A shows that the tubes around the sub-manifolds $\{\boldsymbol{\gamma}(\theta_1, \alpha), \alpha \in [0, 2\pi]\}$ and $\{\boldsymbol{\gamma}(\theta_2, \alpha), \alpha \in [0, 2\pi]\}$ do not self-overlap. We simply check that those tubes do not overlap with each other:

Proposition IV.3: Consider the tube around the manifold $\boldsymbol{\gamma}$ defined in (10) on a cell $\mathcal{D} = [\theta_1, \theta_2] \subsetneq [0, 1]$. Barring the unlikely case where the length of the manifold for fixed α is smaller than ϕ, no edge effects appear if

$$\phi < \phi_{\text{edge}} \triangleq \frac{1}{2} \cos^{-1} \left(\left| \mathbf{s}(\theta_1)^H \mathbf{s}(\theta_2) \right| \right) . \tag{49}$$

In particular, under white noise, if $[\theta_1, \theta_2]$ is a cell $\mathcal{D}_k$ as defined in (6), $\mathbf{s}(\theta_1)^H \mathbf{s}(\theta_2) = 0$, so that $\phi_{\text{edge}} = \pi/4$.

Proof: No edge effect occurs if:

$$\phi < \min_{\alpha_1, \alpha_2} \frac{1}{2} \cos^{-1} \left(\boldsymbol{\gamma}(\theta_1, \alpha_1)^T \boldsymbol{\gamma}(\theta_2, \alpha_2) \right) . \tag{50}$$

With (59), the minimum (50) is reached for $\alpha_1 - \alpha_2 = \angle \mathbf{s}(\theta_1) \mathbf{s}(\theta_2)$. In this case, $\boldsymbol{\gamma}(\theta_1, \alpha_1)^T \boldsymbol{\gamma}(\theta_2, \alpha_2) = \left| \mathbf{s}(\theta_1)^H \mathbf{s}(\theta_2) \right|$, and the rightmost term of (50) reduces to ϕ_{edge} in (49). ■

V. Numerical Results

Let us check the validity of Eq. (16). Fig. 8(a) presents the P_{FA}-threshold relationship given by Eq. (16) and empirically computed thresholds using 10^8 complex circular white Gaussian noise samples for a steering vector size of $N = 10$. The continuous research over the domain $\mathcal{D}$ is replaced by a discrete search using 30 tests in the cell, where $\mathcal{D} = \mathcal{D}_0$.

The formula seems to fit very well when the P_{FA} is low enough (or, equivalently, if the threshold w is high enough), and is quite different from the on-grid relationship, also plotted in Fig. 8, due to the influence of the second term in (15). It is not valid for P_{FA} close to 1 because of overlap (it even exceeds 1). However, such high P_{FA} have no practical interest for standard applications.

It is not trivial to verify the limit overlap value (44) simply by looking at Fig. 8(a): overlap stops having a significant impact on the relationship well before attaining w_{lim}. Let us check our value of w_{lim} by exhibiting a well-chosen point $\underline{\mathbf{u}}$ of the tube belonging to more than one cross-section for a threshold w very close to w_{lim}, with $w < w_{\text{lim}}$, under white noise. Indeed, consider (for any $\theta, \alpha \in \mathcal{D} \times [0, 2\pi]$ since $\boldsymbol{\gamma}$ is shift invariant), the point of the tube

$$\underline{\mathbf{u}} = \cos(\phi)\, \boldsymbol{\gamma}(\theta, \alpha) + \sin(\phi)\, \mathbf{n} , \tag{51}$$

with $\cos \phi = w$ and $\mathbf{n}$ is the unit norm vector such that:

$$\mathbf{n} \propto \boldsymbol{\gamma}(\theta, \alpha) + \sum_{i,j \in [1,2]} \beta_i \beta_j \left(\frac{\partial^2 \boldsymbol{\gamma}}{\partial \mu_i \partial \mu_j} \right),$$

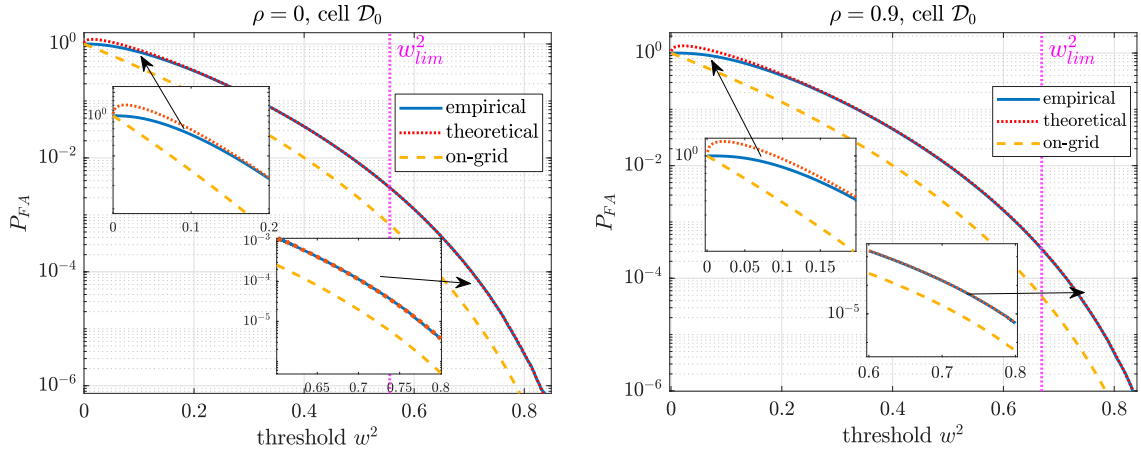

(a) Uncorrelated noise : $\rho = 0$. (b) Highly correlated noise : $\rho = 0.9$.

Fig. 8. Comparison between the theoretical P_{FA}-threshold given in (16) for (a) and (14) for (b) and the empirical Monte Carlo P_{FA}-threshold relationships for $N = 10$ and for several values of ρ (52). The relationship is drawn for the search domain $\mathcal{D}_0$. The on-grid relation (5) is also drawn for comparison purposes. The limit overlap threshold w_{lim} proposed in (24) is in purple.

where $\boldsymbol{\mu}$ is the parametrization defined in (31), and

$$(\beta_1, \beta_2) = \underset{(\beta_1,\beta_2)\in\mathbb{S}^1}{\arg\max} \left\| \sum_{i,j} \beta_i \beta_j \left(\frac{\partial^2 \boldsymbol{\gamma}}{\partial \mu_i \partial \mu_j} \right) \right\|^2,$$

where the right quantity is maximized numerically with $\beta_1 = \sin(\varphi)$, $\beta_2 = \cos(\varphi)$. Note that, using (54), $\mathbf{n}$ is orthogonal to $\boldsymbol{\gamma}(\theta, \alpha)$ so that $\underline{\mathbf{u}}$ is indeed a point of the tube since $\underline{\mathbf{u}}^T \boldsymbol{\gamma}(\theta, \alpha) = \cos\phi = w$ and $\|\underline{\mathbf{u}}\| = 1$. Fig. 9 shows that $\mathbf{u}$ belongs to only one cross-section when $\phi < \phi_{\text{lim}}$ and to three cross-sections when $\phi > \phi_{\text{lim}}$. Indeed, defining the complex vector $\mathbf{u}$ by $\underline{\mathbf{u}} = \begin{bmatrix} \text{Re}(\mathbf{u}) \\ \text{Im}(\mathbf{u}) \end{bmatrix}$, see that the derivative of the product $\left|\mathbf{u}^H \mathbf{s}(\theta + \delta)\right|^2$ vanishes to 0 above the threshold once in the first case, and three times in the second. Using (11), this means that $\underline{\mathbf{u}}^T \dfrac{\partial \boldsymbol{\gamma}}{\partial \theta} = \underline{\mathbf{u}}^T \dfrac{\partial \boldsymbol{\gamma}}{\partial \alpha} = 0$ for 3 values $\xi_i = \left(\theta + \delta_i, \angle \mathbf{u}^H \mathbf{s}(\theta + \delta_i)\right)$ so that $\underline{\mathbf{u}}$ belongs to 3 cross-sections $\mathcal{CS}_{\xi_i}$ according to the definition (23). Even though it is hard to detect visually in Fig. 8(a), overlap occurs right before the limit threshold value w_{lim} found in (42): the limit threshold is very conservative and formula (16) can be used as a good approximate of the true P_{FA} threshold relationship for thresholds well below that.

As mentioned before, test (7) is not CFAR with respect to $\boldsymbol{\Gamma}$ or $\mathcal{D}$. To showcase this, we will use the following well-known model of covariance matrices:

$$\boldsymbol{\Gamma}(\rho) = To\left(\begin{bmatrix} 1 & \rho & \dots \rho^{N-1} \end{bmatrix}\right), \tag{52}$$

where $To(.)$ is the Toeplitz matrix operator, and ρ is a scalar that defines the level of correlation of the noise. It can be seen in Fig. 10 that, for a fixed radius, the surface of the tube around the manifold of whitened signals $\mathbf{s}(\theta)$ for $\theta \in \mathcal{D}$ increases with ρ when $\mathcal{D} = \mathcal{D}_0$, and decreases with ρ for $\mathcal{D} = \mathcal{D}_5$. We thus have also compared the formula (15) with empirical thresholds for colored noise ($\boldsymbol{\Gamma} \neq \mathbf{I}$). Results can be observed in Fig. 8(b) for the edge cell $\mathcal{D}_0$ where detection

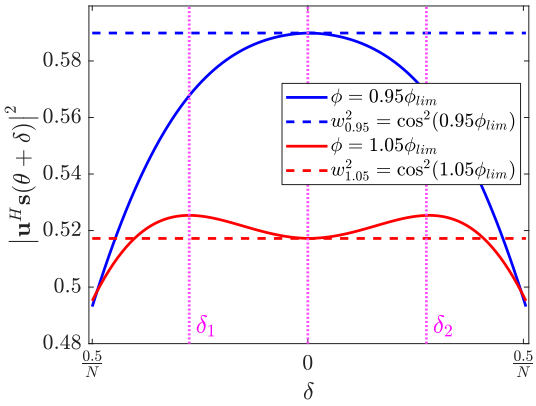

Fig. 9. Illustration of the overlap phenomenon: squared projection of $\mathbf{u}$ defined in (51) on $\mathbf{s}(\theta + \delta)$ for $\theta + \delta \in \mathcal{D}_0$ for two values of ϕ: $\phi = 0.95\phi_{\text{lim}}$ and $\phi = 1.05\phi_{\text{lim}}$.

performance is lower on average. Again, it can be seen that the derived P_{FA}-threshold seems to fit perfectly with what is observed empirically for P_{FA} values that are low enough. Zooming on the leftmost part of the curves, it can be seen that the overlapping phenomenon for low P_{FA} values tends to increase slightly with ρ: the gap between the curves widens slightly and lasts a bit longer as noise becomes more correlated. This is not surprising, as correlated noise bends the manifold, increasing the likeliness of both local and non-local global overlap. The formula is still a good approximation of the P_{FA}-threshold relationship well before the limit threshold for no overlap w_{lim}.

To verify this behavior, we plot the relationship between ρ and the minimum threshold for which there is no overlap w_{lim} computed thanks to (26) on Fig. 11. The components w_{local} and $w_{\text{non-local}}$ are obtained thanks to (40), (36). As we suspected, w_{lim} tends to increase with ρ. The arising of non-local overlap can be explained by looking at the ambiguity maps drawn on Fig. 6: as ρ increases, a side-lobe gets larger

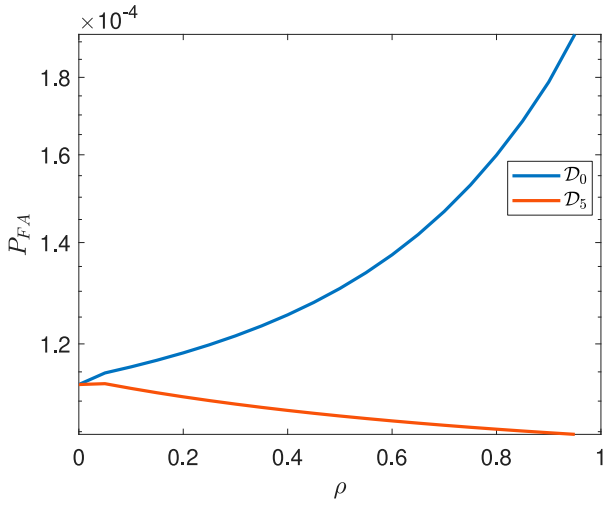

Fig. 10. Evolution of the P_{FA} with ρ for fixed threshold $w^2 = 0.7$, for search domains $\mathcal{D}_0$ and $\mathcal{D}_5$.

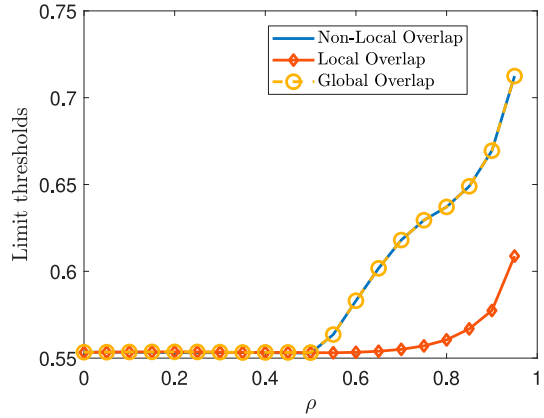

Fig. 11. Comparison of the limit global overlap thresholds w_{lim} (purple), w_{local} (red) and $w_{\text{non-local}}$ (blue) versus ρ obtained with (26), (40) and (36) with $N = 10$, in the cell $\mathcal{D}_0$.

and closer and closer to the origin, increasing the likeliness of non-local overlap.

VI. Conclusion

This article addresses the off-grid detection problem using the NMF-GLRT by finding an analytical P_{FA}-threshold relationship. Several new closed-form expressions under white noise have been expressed. We then analyzed its domain of validity thanks to the application of results on the overlap phenomena for tubes around multi-dimensional manifolds to the off-grid signal model. This analysis shows that our relationship is valid for most common radar applications for which the P_{FA} is low enough. Finally, simulations comparing our theoretical relationship with empirical thresholds computed with Monte Carlo trials validate our results.

At first glance, the tools used in this paper cannot be applied to the analysis of the P_D of the off-grid GLRT or the extension of the P_{FA}-threshold relationship to the adaptive case for $\mathbf{\Gamma}$ unknown. This is because, in both cases, the distribution of the whitened received vector is not uniform over the unit sphere, and so the probabilities cannot be obtained directly as a ratio of surfaces anymore.

Appendix

In the first section of the appendix, we prove that the tube $\mathcal{T}_{\text{on-grid}}$, defined in (13) for fixed θ, does not overlap. Then, we provide proofs for the corollaries of Section IV.

A. On the Absence of Overlap of the Tube $\mathcal{T}_{\text{on-grid}}$ (13) for Fixed θ

Since $\left\| \frac{\partial \boldsymbol{\gamma}(\theta,\alpha)}{\partial \alpha} \right\| = 1$, $\boldsymbol{\gamma}(\theta,.)$ is parameterized by arc length. The radius of first curvature is then defined as $\rho = \left\| \frac{\partial^2 \boldsymbol{\gamma}(\theta,\alpha)}{\partial \alpha^2} \right\|^{-1} = 1$. Then, since $\sin(\cos^{-1} w) < 1$ for all w, there is no local overlap according to (9).

Let us prove there is no non-local overlap either by searching the pairs of points of interest (α, α') in Ξ, that verify:

$$\boldsymbol{\gamma}(\theta,\alpha')^T \dot{\boldsymbol{\gamma}}(\theta,\alpha) = \boldsymbol{\gamma}(\theta,\alpha)^T \dot{\boldsymbol{\gamma}}(\theta,\alpha') = 0\,.$$

Those conditions imply that:

$$(\cos\alpha' \boldsymbol{\gamma}_1(\theta) + \sin\alpha' \boldsymbol{\gamma}_2(\theta))^T (\cos\alpha \boldsymbol{\gamma}_2(\theta) - \sin\alpha \boldsymbol{\gamma}_1(\theta)) = 0\,,$$

that leads to the condition:

$$-\cos\alpha' \sin\alpha \|\gamma_1(\theta)\| + \sin\alpha' \cos\alpha \|\gamma_2(\theta)\| = 0\,,$$

and equivalently: $\sin(\alpha - \alpha') = 0$.

Thus, the set Ξ is defined as:

$$\begin{aligned}\Xi &= \{(\alpha,\alpha') : \alpha \neq \alpha', \sin(\alpha-\alpha') = 0\}\,,\\ &= \{(\alpha, \alpha+\pi), \alpha \in [0,\pi]\}\,.\end{aligned}$$

For any $\alpha \in [0,\pi]$, we have $\boldsymbol{\gamma}(\alpha,\theta)^T \boldsymbol{\gamma}(\alpha+\pi,\theta) = -1$, so that $\phi_{\text{non-local}} = \frac{1}{2}\arccos(-1) = \frac{\pi}{2}$ according to (36): there is no non-local overlap for $\mathcal{T}_{\text{on-grid}}$. Thus, $w_{\text{lim}} = \cos\phi_{\text{lim}} = 0$ and the surface given by (13) is exact for any threshold w.

B. Proof of Proposition IV.1

Proof: Let $\boldsymbol{\gamma}(\boldsymbol{\xi})^T \boldsymbol{\gamma}(\boldsymbol{\xi}') = f(\boldsymbol{\xi} - \boldsymbol{\xi}')$. The quantity $h(\boldsymbol{\xi}, \boldsymbol{\xi}')$ depends on $\boldsymbol{\xi}$ and $\boldsymbol{\xi}'$ through $\boldsymbol{\gamma}(\boldsymbol{\xi})^T \boldsymbol{\gamma}(\boldsymbol{\xi}') = f(\boldsymbol{\xi} - \boldsymbol{\xi}')$ in the denominator, and, by the way of $\mathbf{P}_{\boldsymbol{\xi}'}$ in the numerator, $\boldsymbol{\gamma}(\boldsymbol{\xi})^T \frac{\partial \boldsymbol{\gamma}(\boldsymbol{\xi}')}{\partial \xi'_k}$ and $\frac{\partial \boldsymbol{\gamma}(\boldsymbol{\xi})^T}{\partial \xi_i} \frac{\partial \boldsymbol{\gamma}(\boldsymbol{\xi}')}{\partial \xi'_j}$ for $k \in [1, M]$ and $(i,j) \in [1,M]^2$. By using the derivatives of f, it can be shown that those two terms and h depend only on the difference $\boldsymbol{\xi} - \boldsymbol{\xi}'$. ■

C. Proof of Corollary IV.1.2

To prove Corollary IV.1.2, we need to introduce the following lemma on the existence of the parametrization $\boldsymbol{\mu}$:

Lemma A.1: Let $\boldsymbol{\gamma}(\boldsymbol{\xi})$ be a M-dimensional shift-invariant manifold. The parametrization $\boldsymbol{\mu}$ chosen in (31) is well defined, and its first fundamental form is equal to $\mathbf{I}$:

$$\frac{\partial \boldsymbol{\gamma}^T}{\partial \mu_i} \frac{\partial \boldsymbol{\gamma}}{\partial \mu_j} = \delta_{i,j}\,.$$

Proof: Consider $\mathbf{G} = (g_{ij})_{1\leq i,j\leq N}$ defined as in (29). Note that by differentiating $\boldsymbol{\gamma}^T\boldsymbol{\gamma} = 1$ twice, we have:

$$\boldsymbol{\gamma}^T \frac{\partial^2 \boldsymbol{\gamma}}{\partial \xi_i \partial \xi_j} = -\frac{\partial \boldsymbol{\gamma}}{\partial \xi_i}^T \frac{\partial \boldsymbol{\gamma}}{\partial \xi_j}. \tag{53}$$

Let $f(\boldsymbol{\xi} - \boldsymbol{\xi}') = \boldsymbol{\gamma}(\boldsymbol{\xi})^T \boldsymbol{\gamma}(\boldsymbol{\xi}')$. It can be rewritten equivalently $f(\mathbf{y}) = \boldsymbol{\gamma}(\boldsymbol{\xi})^T \boldsymbol{\gamma}(\boldsymbol{\xi} + \mathbf{y})$, which gives, using (53):

$$g_{ij} = \frac{\partial \boldsymbol{\gamma}^T}{\partial \xi_i} \frac{\partial \boldsymbol{\gamma}}{\partial \xi_j} = -\frac{\partial^2 f}{\partial y_i \partial y_j}\Big|_{\mathbf{y}=\mathbf{0}}.$$

Thus, the coefficients g_{ij} do not depend on $\boldsymbol{\xi}$, and so neither does $\mathbf{G}$. We can define $\mathbf{G}^{1/2}$ as in (30) since $\mathbf{G}$ is positive definite. Then, the parametrization (31) in the corollary is well defined, so that $\boldsymbol{\xi} = \mathbf{G}^{-1/2}\boldsymbol{\mu}$. Then:

$$\begin{aligned}
\frac{\partial \boldsymbol{\gamma}^T}{\partial \mu_i} \frac{\partial \boldsymbol{\gamma}}{\partial \mu_j} &= \sum_{m,k} \frac{\partial \xi_k}{\partial \mu_i} \frac{\partial \boldsymbol{\gamma}^T}{\partial \xi_k} \frac{\partial \boldsymbol{\gamma}}{\partial \xi_m} \frac{\partial \xi_m}{\partial \mu_j}, \\
&= \sum_{m,k} G^{-1/2}_{k,i} G_{k,m} G^{-1/2}_{m,j}, \\
&= \left(\mathbf{G}^{-T/2}\mathbf{G}\mathbf{G}^{-1/2}\right)_{i,j}, \\
&= \delta_{i,j}.
\end{aligned}$$

■

The following proves Corollary IV.1.2:

Proof: Equation (32) has been proved in the above lemma. Let us prove (33). First, note that differentiating $\boldsymbol{\gamma}^T\boldsymbol{\gamma} = 1$ twice yields:

$$\boldsymbol{\gamma}^T \frac{\partial^2 \boldsymbol{\gamma}}{\partial \mu_i \partial \mu_j} = -\frac{\partial \boldsymbol{\gamma}}{\partial \mu_i} \frac{\partial \boldsymbol{\gamma}}{\partial \mu_j} = -\delta_{ij}. \tag{54}$$

Next, let us introduce Christoffel symbols of the first kind:

$$\Gamma_{ijk} = \frac{\partial^2 \boldsymbol{\gamma}^T}{\partial \mu_i \partial \mu_j} \frac{\partial \boldsymbol{\gamma}}{\partial \mu_k}. \tag{55}$$

It can be easily verified that those symbols can be expressed as a function of the derivatives of the first fundamental form $\mathbf{G}' = \left(g'_{ij}\right)_{1\leq i,j\leq N}$:

$$\Gamma_{ijk} = \frac{1}{2}\left(\frac{\partial g'_{ik}}{\partial \mu_j} + \frac{\partial g'_{jk}}{\partial \mu_i} - \frac{\partial g'_{ij}}{\partial \mu_k}\right),$$

which gives, since according to (32) $g'_{ij} = \delta_{i,j}$:

$$\Gamma_{ijk} = 0. \tag{56}$$

Let us now consider Equation (28) with parametrization μ. The denominator reduces to 1:

$$\sum_{i,j} \beta_i \beta_j \frac{\partial \boldsymbol{\gamma}^T}{\partial \mu_i} \frac{\partial \boldsymbol{\gamma}}{\partial \mu_j} = \sum_{i,j} \beta_i \beta_j \, \delta_{i,j} = \sum_i \beta_i^2 = 1.$$

We thus have:

$$\begin{aligned}
\cot^2 \phi_{\text{local}} &= \sup_{\beta \in \mathbb{S}^{M-1}} \left\| \sum_{i,j} \beta_i \beta_j \left(\mathbf{I} - \mathbf{P}_\mu\right) \frac{\partial^2 \boldsymbol{\gamma}}{\partial \mu_i \partial \mu_j} \right\|^2, \\
&= \sup_{\beta \in \mathbb{S}^{M-1}} \left(\left\| \sum_{i,j} \beta_i \beta_j \frac{\partial^2 \boldsymbol{\gamma}}{\partial \mu_i \partial \mu_j} \right\|^2 \right. \\
&\quad \left. - \left\| \mathbf{P}_\mu \sum_{i,j} \beta_i \beta_j \frac{\partial^2 \boldsymbol{\gamma}}{\partial \mu_i \partial \mu_j} \right\|^2 \right),
\end{aligned} \tag{57}$$

where the maximization on μ has been omitted since the manifold $\boldsymbol{\gamma}$ is shift-invariant. $\left(\boldsymbol{\gamma}, \frac{\partial \boldsymbol{\gamma}}{\partial \mu_1}, \ldots, \frac{\partial \boldsymbol{\gamma}}{\partial \mu_M}\right)$ forms an orthonormal family so that the second term of (57) is, with Pythagoras's theorem:

$$\begin{aligned}
&\left\| \mathbf{P}_\mu \sum_{i,j} \beta_i \beta_j \frac{\partial^2 \boldsymbol{\gamma}}{\partial \mu_i \partial \mu_j} \right\|^2 \\
&= \left| \sum_{i,j} \beta_i \beta_j \boldsymbol{\gamma}^T \frac{\partial^2 \boldsymbol{\gamma}}{\partial \mu_i \partial \mu_j} \right|^2 + \sum_k \left| \sum_{i,j} \beta_i \beta_j \frac{\partial \boldsymbol{\gamma}^T}{\partial \mu_k} \frac{\partial^2 \boldsymbol{\gamma}}{\partial \mu_i \partial \mu_j} \right|^2, \\
&= \left| \sum_{i,j} \beta_i \beta_j \delta_{i,j} \right|^2 + \sum_k \left| \sum_{i,j} \beta_i \beta_j \Gamma_{ijk} \right|^2, \\
&= 1,
\end{aligned}$$

using (54), (55) and (56). ■

D. Proof of Corollary IV.1.5

To prove Corollary IV.1.5, we must introduce the following Lemma to use Corollary IV.1.2.

Lemma A.2: Under white noise ($\boldsymbol{\Gamma} = \mathbf{I}$), the manifold $\boldsymbol{\gamma}$ as defined in (10) is shift invariant.

Proof: The complex manifold $\mathbf{s}(\theta)$ can be expressed as:

$$\begin{aligned}
\mathbf{s}(\theta)^H \mathbf{s}(\theta') &= \frac{1}{\sqrt{N}} \sum_{k=0}^{N-1} e^{2i\pi k(\theta' - \theta)}, \\
&= f(\theta - \theta'), \\
&= \mathrm{Re}\left(f(\theta - \theta')\right) + i \, \mathrm{Im}\left(f(\theta - \theta')\right).
\end{aligned}$$

where $f(\theta - \theta') = e^{i\pi(N-1)(\theta' - \theta)} \dfrac{\sin(\pi N(\theta' - \theta))}{\sin(\pi N(\theta' - \theta))}$. Thus, one finds:

$$\begin{aligned}
\boldsymbol{\gamma}(\theta, \alpha)^T \boldsymbol{\gamma}(\theta', \alpha') &= \cos(\alpha - \alpha') \, \mathrm{Re}\left(f(\theta - \theta')\right) \\
&\quad + \sin(\alpha - \alpha') \, \mathrm{Im}\left(f(\theta - \theta')\right),
\end{aligned}$$

which shows the manifold of interest $\boldsymbol{\gamma}$ is shift-invariant. ■

We are now able to prove Corollary IV.1.5:

Proof: In order to find a parametrization $\boldsymbol{\mu}$ of $\boldsymbol{\gamma}$ satisfying the condition (32), one can use the following vector $\mathbf{d}'(v)$ instead of $\mathbf{d}(\theta)$ in the derivations, changing the origin of time ($\mathbf{d}$ and $\mathbf{d}'$ model the same problem):

$$\left(\mathbf{d}'(v)\right)_n = \frac{1}{\sqrt{N}} \exp\left(2i\pi \left(n - \frac{N-1}{2}\right) l^{-1} v\right),$$

for $0 \leq n \leq N-1$ and where

$$l = \pi \sqrt{\frac{N^2 - 1}{3}}, \quad v = l\,\theta.$$

The parametrization $\boldsymbol{\mu} = (v, \alpha)$ for $\boldsymbol{\gamma}$ written with $\mathbf{d}'$ verifies condition (32). Let us compute (33):

$$\begin{aligned}
&\frac{\partial^2 \boldsymbol{\gamma}^T}{\partial^2 v}\frac{\partial^2 \boldsymbol{\gamma}}{\partial^2 v} = C,\\
&\frac{\partial^2 \boldsymbol{\gamma}^T}{\partial v\,\partial \alpha}\frac{\partial^2 \boldsymbol{\gamma}}{\partial^2 v} = \frac{\partial^2 \boldsymbol{\gamma}^T}{\partial v\,\partial \alpha}\frac{\partial^2 \boldsymbol{\gamma}}{\partial^2 \alpha} = 0\,,\\
&\frac{\partial^2 \boldsymbol{\gamma}^T}{\partial^2 v}\frac{\partial^2 \boldsymbol{\gamma}}{\partial^2 \alpha} = \frac{\partial^2 \boldsymbol{\gamma}^T}{\partial v\,\partial \alpha}\frac{\partial^2 \boldsymbol{\gamma}}{\partial v\,\partial \alpha} = \frac{\partial^2 \boldsymbol{\gamma}^T}{\partial^2 \alpha}\frac{\partial^2 \boldsymbol{\gamma}}{\partial^2 \alpha} = 1\,,
\end{aligned}$$

where C has been defined in (43). Injecting in (33), with $\beta_1 = \cos\varphi$, $\beta_2 = \sin\varphi$ and maximizing on φ, we get:

$$\begin{aligned}
\cot^2\phi_{\text{local}} &= \max_{\varphi} C\cos^4\varphi + 6\cos^2\varphi\sin^2\varphi + \sin^4\varphi - 1,\\
&= \max_{\varphi} (C-5)\cos^4\varphi + 4\cos^2\varphi. \qquad (58)
\end{aligned}$$

The maximum is obtained for $\cos^2\varphi = \dfrac{2}{5-C}$. Then, injecting this value in (58) and simplifying, we obtain:

$$\cot^2\phi_{\text{local}} = \frac{4}{5-C}\,.$$

Since $w_{\text{local}}^2 = \cos^2\left(\tan^{-1}\dfrac{1}{\sqrt{\cot^2\phi_{\text{local}}}}\right)$, result (42) holds. ■

E. Proof of Corollary IV.1.6

Proof: First, see that:

$$\begin{aligned}
\boldsymbol{\gamma}(\theta,\alpha)^T\boldsymbol{\gamma}(\theta',\alpha') &= \cos(\alpha-\alpha')\,\mathrm{Re}\left(\mathbf{s}(\theta)^H\mathbf{s}(\theta')\right)\\
&\quad + \sin(\alpha-\alpha')\,\mathrm{Im}\left(\mathbf{s}(\theta)^H\mathbf{s}(\theta')\right),\\
&= \mathrm{Re}\left(e^{-i(\alpha-\alpha')}\,\mathbf{s}(\theta)^H\mathbf{s}(\theta')\right),\\
&\le \left|\mathbf{s}(\theta)^H\,\mathbf{s}(\theta')\right|, \qquad (59)
\end{aligned}$$

with the equality attained for $\alpha - \alpha' = \angle\mathbf{s}(\theta)^H\mathbf{s}(\theta')$. This implies that the only points of Ξ worth investigating are the pairs of points $(\theta,\alpha),(\theta',\alpha')$ with (α,α') chosen arbitrarily so that $\alpha - \alpha' = \angle\mathbf{s}(\theta)^H\mathbf{s}(\theta')$ and (θ,θ') being a critical point of the quantity $\left|\mathbf{s}(\theta)^H\,\mathbf{s}(\theta')\right|$ which define the set Ξ' in (45). ■

REFERENCES

[1] L. L. Scharf and C. Demeure, *Statistical Signal Processing: Detection, Estimation, and Time Series Analysis*. Englewood Cliffs, NJ, USA: Prentice-Hall, 1991.

[2] F. Pascal, J.-P. Ovarlez, P. Forster, and P. Larzabal, "On a SIRV-CFAR detector with radar experimentations in impulsive noise," in *Proc. Eur. Signal Process. Conf. (EUSIPCO)*, Florence, Italy, Sep. 2006.

[3] E. Ollila, D. E. Tyler, V. Koivunen, and H. V. Poor, "Complex Elliptically Symmetric distributions: Survey, new results and applications," *IEEE Trans. Signal Process.*, vol. 60, no. 11, pp. 5597–5625, Nov. 2012.

[4] O. Rabaste, J. Bosse, and J.-P. Ovarlez, "Off-grid target detection with normalized matched subspace filter," in *Proc. 24th Eur. Signal Process. Conf. (EUSIPCO)*, Aug. 2016, pp. 1926–1930.

[5] A. De Maio, "Robust adaptive radar detection in the presence of steering vector mismatches," *IEEE Trans. Aerosp. Electron. Syst.*, vol. 41, no. 4, pp. 1322–1337, Oct. 2005.

[6] O. Besson, "Detection of a signal in linear subspace with bounded mismatch," *IEEE Trans. Aerosp. Electron. Syst.*, vol. 42, no. 3, pp. 1131–1139, Jul. 2006.

[7] O. Besson, "Adaptive detection with bounded steering vectors mismatch angle," *IEEE Trans. Signal Process.*, vol. 55, no. 4, pp. 1560–1564, Apr. 2007.

[8] F. Bandiera, A. De Maio, and G. Ricci, "Adaptive CFAR radar detection with conic rejection," *IEEE Trans. Signal Process.,* vol. 55, no. 6, pp. 2533–2541, Jun. 2007.

[9] A. De Maio, S. De Nicola, Y. Huang, S. Zhang, and A. Farina, "Adaptive detection and estimation in the presence of useful signal and interference mismatches," *IEEE Trans. Signal Process., IEEE Trans.*, vol. 57, no. 2, pp. 436–450, Feb. 2009.

[10] A. De Maio, Y. Huang, D. P. Palomar, S. Zhang, and A. Farina, "Fractional QCQP with applications in ML steering direction estimation for radar detection," *IEEE Trans. Signal Process.,* vol. 59, no. 1, pp. 172–185, Jan. 2011.

[11] F. Bandiera, D. Orlando, and G. Ricci, *Advanced Radar Detection Schemes Under Mismatched Signal Models*. San Rafael, CA, USA: Morgan & Claypool, 2009.

[12] F. Bandiera, O. Besson, and G. Ricci, "An ABORT-like detector with improved mismatched signals rejection capabilities," *IEEE Trans. Signal Process.,* vol. 56, no. 1, pp. 14–25, Jan. 2008.

[13] J. Bosse, O. Rabaste, and J.-P. Ovarlez, "Adaptive subspace detectors for off-grid mismatched targets," in *Proc. IEEE Int. Conf. Acoust., Speech Signal Process. (ICASSP)*, 2020, pp. 4777–4780.

[14] G. Tang, B. N. Bhaskar, P. Shah, and B. Recht, "Compressed sensing off the grid," *IEEE Trans. Inf. Theory*, vol. 59, no. 11, pp. 7465–7490, Nov. 2013.

[15] M. Lasserre, S. Bidon, O. Besson, and F. Le Chevalier, "Bayesian sparse Fourier representation of off-grid targets with application to experimental radar data," *Signal Process.*, vol. 111, pp. 261–273, Jun. 2015.

[16] J. Dai, X. Bao, W. Xu, and C. Chang, "Root sparse Bayesian learning for off-grid DOA estimation," *IEEE Signal Process. Lett.*, vol. 24, no. 1, pp. 46–50, Jan. 2017.

[17] P. Chen, Z. Cao, Z. Chen, and X. Wang, "Off-grid DOA estimation using sparse Bayesian learning in MIMO radar with unknown mutual coupling," *IEEE Trans. Signal Process.,* vol. 67, no. 1, pp. 208–220, Jan. 2019.

[18] I. Selin, "Detection of coherent radar returns of unknown Doppler shift," *IEEE Trans. Inf. Theory*, vol. IT-11, no. 3, pp. 396–400, Jul. 1965.

[19] L. Brennan, I. Reed, and W. Sollfrey, "A comparison of average-likelihood and maximum-likelihood ratio tests for detecting radar targets of unknown Doppler frequency," *IEEE Trans. Inf. Theory,* vol. IT-14, no. 1, pp. 104–110, Jan. 1968.

[20] A. Aubry, A. De Maio, S. Marano, and M. Rosamilia, "Single-pulse simultaneous target detection and angle estimation in a multichannel phased array radar," *IEEE Trans. Signal Process.,* vol. 68, pp. 6649–6664, 2020.

[21] A. Aubry, A. De Maio, L. Lan, and M. Rosamilia, "Adaptive radar detection and bearing estimation in the presence of unknown mutual coupling," *IEEE Trans. Signal Process.,* vol. 71, pp. 1248–1262, 2023.

[22] O. Besson, L. L. Scharf, and F. Vincent, "Matched direction detectors and estimators for array processing with subspace steering vector uncertainties," *IEEE Trans. Signal Process.,* vol. 53, no. 12, pp. 4453–4463, Dec. 2005.

[23] L. L. Scharf and B. Friedlander, "Matched subspace detectors," *IEEE Trans. Signal Process.*, vol. 42, no. 8, pp. 2146–2157, Aug. 1994.

[24] P. Develter, J. Bosse, O. Rabaste, P. Forster, and J.-P. Ovarlez, "Off-grid radar target detection with the normalized matched filter: A monopulse-based detection scheme," in *Proc. IEEE Statist. Signal Process. Workshop (SSP)*, Piscataway, NJ, USA: IEEE Press, 2021, pp. 226–230.

[25] A. De Maio, S. De Nicola, A. Farina, and S. Iommelli, "Adaptive detection of a signal with angle uncertainty," *IET Radar Sonar Navig.*, vol. 4, no. 4, pp. 537–547, 2010.

[26] S. O. Rice, "Mathematical analysis of random noise," *Bell Syst. Tech. J.*, vol. 23, no. 3, pp. 282–332, 1944.

[27] R. J. Adler, "On excursion sets, tube formulas and maxima of random fields," *Ann. Appl. Probab.*, vol. 10, no. 1, pp. 1–74, Feb. 2000.

[28] K. J. Worsley, "Estimating the number of peaks in a random field using the Hadwiger characteristic of excursion sets, with applications to medical images," *Ann. Statist.*, vol. 23, no. 2, pp. 640–669, Apr. 1995.

[29] S. D. Hayward, "CFAR detection of targets with unknown Doppler shifts," *Electron. Lett.*, vol. 39, no. 6, pp. 1–2, 2003.

[30] H. Hotelling, "Tubes and spheres in n-spaces, and a class of statistical problems," *Amer. J. Math.*, vol. 61, no. 2, pp. 440–460, 1939.

[31] I. Johnstone and D. Siegmund, "On Hotelling's formula for the volume of tubes and Naiman's inequality," *Ann. Statist.*, vol. 17, no. 1, pp. 184–194, Mar. 1989.

[32] P. Develter, J. Bosse, O. Rabaste, P. Forster, and J.-P. Ovarlez, "On the false alarm probability of the normalized matched filter for off-grid target detection," in *Proc. IEEE Int. Conf. Acoust., Speech Signal Process. (ICASSP)*, Piscataway, NJ, USA: IEEE Press, 2022, pp. 5782–5786.

[33] S. Johansen and I. M. Johnstone, "Hotelling's theorem on the volume of tubes: Some illustrations in simultaneous inference and data analysis," *Ann. Statist.*, vol. 18, no. 2, pp. 652–684, 1990.
[34] S. Kuriki and A. Takemura, "Tail probabilities of the maxima of multilinear forms and their applications," *Ann. Statist.*, vol. 29, no. 2, pp. 328–371, Apr. 2001.
[35] E. Conte, M. Lops, and G. Ricci, "Asymptotically optimum radar detection in compound-Gaussian clutter," *IEEE Trans. Aerosp. Electron. Syst.*, vol. 31, no. 2, pp. 617–625, Apr. 1995.
[36] O. Rabaste and N. Trouvé, "Geometrical design of radar detectors in moderately impulsive noise," *IEEE Trans. Aerosp. Electron. Syst.*, vol. 50, no. 3, pp. 1938–1954, 2014.
[37] E. Jacobsen and P. Kootsookos, "Fast, accurate frequency estimators [DSP tips & tricks]," *IEEE Signal Process. Mag.*, vol. 24, no. 3, pp. 123–125, May 2007.
[38] M. Hohenwarter, *GeoGebra - ein Softwaresystem für dynamische Geometrie und Algebra der Ebene*. Salzburg, Austria: University of Salzburg, 2002.
[39] M. Knowles and D. Siegmund, "On Hotelling's approach to testing for a nonlinear parameter in regression," *Int. Statist. Rev./Revue Internationale de Statistique*, vol. 57, no. 3, pp. 205–220, Dec. 1989.

Pierre Develter received the M.Sc. degree from IMT Atlantique, Brest, France, in 2020, and the Ph.D. degree in Signal Processing from Centrale-Supélec, Université Paris-Saclay, France in partnership with ONERA, in 2023. His research interests include detection and information theory, as well as radar signal processing.

Jonathan Bosse received the M.Sc. degree from Centrale Marseille, Marseille, France, in 2008, and the Ph.D. degree in electrical engineering from Ecole Normale Supérieure de Cachan, Cachan, France, in 2012. From 2009 to 2012, he worked toward the Ph.D. degree through a CIFRE convention between Thales Communications and Ecole Normale Supérieure de Cachan. He was then Postdoctorate with TU Delft, The Netherlands in the Microwave Sensing, Signals and Systems group during two years. In 2014, he joined ONERA, The French Aerospace Lab. His research interests include estimation and detection in radar and array processing.

Olivier Rabaste received the Engineering degree in telecommunications from the Ecole Nationale Supérieure des Télécommunications de Bretagne, Brest, France, in 2003, the M.S. degree in digital communications systems and technologies with distinction from the Chalmers University of Technology, Göteborg, Sweden, in 2003, and the Ph.D. degree from the Ecole Nationale Supérieure des Télécommunications de Bretagne, in 2006. He is currently a Research Engineer with ONERA, the French Aerospace Lab since 2008. His research interests include detection, estimation and tracking for radar applications.

Philippe Forster was born in Brest, France, in 1960. He received the Agrégation de physique appliquée degree from the Ecole Normale Supérieure de Cachan, Cachan, France, in 1983, and the Ph.D. degree in electrical engineering from the Université de Rennes, Rennes, France, in 1988. He is currently a Professor of electrical engineering with Paris Nanterre University, and a Member of the Systemes et Applications des Technologies de l'Information et de l'Enérgie Laboratory, Ecole Normale Supérieure Paris-Saclay. His research interests include estimation and detection theory with applications to array processing, radar, and digital communications.

Jean-Philippe Ovarlez was born in Denain, France in 1963. He received the Engineering degree from Ecole Supérieure d'Electronique Automatique et Informatique (ESIEA), Paris, France, and the Diplôme d'Etudes Approfondies degree in signal processing from the University of Paris XI, Orsay, France, and the Ph.D. degree in physics from the University of Paris VI, Paris, France, jointly, in 1987 and 1992, respectively. In 2011, he obtained a Research Directorship Habilitation (HDR) thesis in signal processing from the University of Paris-Sud and his qualification for the University Professor position. In 1992, he joined the Electromagnetic and Radar Division of the French Aerospace Lab (ONERA), Palaiseau, France, where he is currently a Research Director. Since 2008, he has been attached part-time to Centrale-Supélec SONDRA Lab for the supervision of signal processing activities. In 2015, he became a Special Area Team (SAT) Member in Theoretical and Methodological Trends in Signal Processing (TMTSP), EURASIP, and treasurer of the IEEE GRSS French Chapter in 2016. His research interests include statistical signal processing for radar and SAR applications such as time-frequency, imaging, detection, and parameter estimation.